Spring 5-31-2006

Novel characterization of materials using THz spectroscopic techniques

Amartya Sengupta
New Jersey Institute of Technology

ABSTRACT

NOVEL CHARACTERIZATION OF MATERIALS USING THz SPECTROSCOPIC TECHNIQUES

by
Amartya Sengupta

Significant scientific and technical challenges within the terahertz (THz) frequency regime have recently motivated an array of new research activities. This involves numerous applications of this region of the electromagnetic spectrum between approximately 100 GHz (3mm) and 3 THz (100 μm) for both spectroscopy and imaging purposes. THz time domain spectroscopy is unique in that the time domain waveforms are measured and the complex optical constants are deduced directly without resorting to the Kramers-Kronig Analysis.

In this work, THz spectroscopy has been used to characterize different types of materials. Materials investigated consisted of semiconductors, gate dielectric materials, high energetic materials and cyclic olefin polymers. Besides demonstrating that surface roughness affects the THz transmission, one of the most significant contributions of this work has been to deduce the number of defect states in buried layers. The study also attempts to develop a preliminary model based on effective medium approximations to predict the thickness of the interfacial layer which might be having a myriad of applications in the semiconductor industry. The characterization of a cyclic olefin polymer showed that it is probably the "candidate of the future" for fabrication of far infrared optics mainly because of its low loss and transparency in both the visible and far infrared region of the EM spectrum.

NOVEL CHARACTERIZATION OF MATERIALS USING THz SPECTROSCOPIC TECHNIQUES

by
Amartya Sengupta

A Dissertation
Submitted to the Faculty of
New Jersey Institute of Technology and
Rutgers, The State University of New Jersey – Newark
in Partial Fulfillment of the Requirements for the Degree of
Doctor of Philosophy in Applied Physics

Federated Physics Department

May 2006

APPROVAL PAGE

NOVEL CHARACTERIZATION OF MATERIALS USING THz SPECTROSCOPIC TECHNIQUES

Amartya Sengupta

Dr. John F. Federici, Dissertation Advisor — Date
Professor of Physics and Biomedical Optics, New Jersey Institute of Technology, NJ

Dr. Robert B. Barat, Committee Member — Date
Professor of Chemical Engineering, New Jersey Institute of Technology, NJ

Dr. Dale E. Gary, Committee Member — Date
Professor of Physics, New Jersey Institute of Technology, NJ

Dr. Richard Mendelsohn, Committee Member — Date
Professor of Chemistry, Rutgers, The State University of New Jersey-Newark, NJ

Dr. Nuggehalli M. Ravindra, Committee Member — Date
Professor of Physics, New Jersey Institute of Technology, NJ

Dr. Pradyumna K. Swain, Committee Member — Date
Technical Manager, Sarnoff Imaging Systems, Princeton, NJ

BIOGRAPHICAL SKETCH

Author: Amartya Sengupta

Degree: Doctor of Philosophy

Date: May 2006

Undergraduate and Graduate Education:

- Doctor of Philosophy in Applied Physics,
  New Jersey Institute of Technology, Newark, NJ, 2006

- Master of Science in Physics,
  Indian Institute of Technology, Delhi, New Delhi, India, 2002

- Bachelor of Science in Physics,
  St. Xavier's College, University of Calcutta, Calcutta, India, 2000

Major: Applied Physics

Presentations and Publications:

Aparajita Bandyopadhyay, Amartya Sengupta, R.B. Barat, D.E. Gary, Z. Michalopoulou and J.F. Federici,
"Interferometric THz Imaging for detection of lethal agents using artificial neural network analysis," *Int. J. Infrared Millimeter Waves,* (accepted), 2006.

A.M. Sinyukov, Aparajita Bandyopadhyay, Amartya Sengupta, R.B. Barat, D.E. Gary, Z. Michalopoulou, D.A. Zimdars and J.F. Federici,
"Terahertz interferometric and synthetic aperture imaging," *Proc. SPIE* **6212**, (in press), 2006.

Amartya Sengupta, Aparajita Bandyopadhyay, J.F. Federici, H. Grebel and D. Pham,
"A non-contact characterization technique of the defect states of high k dielectrics using THz radiation," *Proc. IEEE Sarnoff Symposium*, (in press), 2006

Aparajita Bandyopadhyay, A.M. Sinyukov, Amartya Sengupta, R.B. Barat, D.E. Gary, Z. Michalopoulou and J.F. Federici,
"Interferometric THz Imaging for detection of lethal agents using artificial neural network analysis," *Proc. IEEE Sarnoff Symposium*, (in press), 2006.

Amartya Sengupta, Aparajita Bandyopadhyay, Hakan Altan, H. Grebel, D. Pham and J.F. Federici,
"Terahertz Spectroscopy as a non contact estimation technique of defect states in high dielectric constant materials," *APS March Meeting*, G 17.00004, Baltimore, MD, 14 March 2006.

Aparajita Bandyopadhyay, Amartya Sengupta, V. Johnson, J.A. Harrington and J.F. Federici,
"THz time domain spectroscopy of hollow polycarbonate waveguides," *APS March Meeting*, N17.00010, Baltimore, MD, 15 March 2006.

Amartya Sengupta, Aparajita Bandyopadhyay, J.F. Federici, D.E. Gary and R.B. Barat,
"THz Reflection Spectroscopy of Composition C-4 and its detection through interferometric imaging," *Proc. SPIE* **6120**, *Terahertz and Gigahertz Electronics and Photonics V,* 61200A, 2006.

Aparajita Bandyopadhyay, Amartya Sengupta, Valencia Johnson, J.A. Harrington and J.F. Federici,
"Characterization of hollow polycarbonate waveguides using THz time domain spectroscopy," *Proc. SPIE* **6120**, *Terahertz and Gigahertz Electronics and Photonics V,* 61200B, 2006.

Aparajita Bandyopadhyay, Amartya Sengupta, R.B. Barat, D.E. Gary, and J.F. Federici,
"Grain size dependent scattering studies of common materials using THz time domain techniques," *Proc. SPIE* **6120**, *Terahertz and Gigahertz Electronics and Photonics V,* 61200H, 2006.

Amartya Sengupta, Aparajita Bandyopadhyay, J.F. Federici, D.E. Gary and R.B. Barat,
"Spectral identification of granular solids in the terahertz range," *Int. J. Infrared Millimeter Waves,* (under review), 2006.

Amartya Sengupta, Aparajita Bandyopadhyay, J.F. Federici and N.M. Ravindra,
"Optical properties of Silicon in the terahertz regime", *Solid State Electron.,* (under review), 2006.

Aparajita Bandyopadhyay, A. Stepanov, B. Schulkin, M.D. Federici, Amartya Sengupta, J.F. Federici, D.E. Gary, R.B. Barat, Z. Michalopoulou and D. Zimdars,
"THz interferometric and synthetic aperture imaging," *J. Opt. Soc. Am. A*, (in press), 2006.

Amartya Sengupta, Hakan Altan, Aparajita Bandyopadhyay, J.F. Federici, H. Grebel and D. Pham,
"Investigation of Defect States of HfO_2 and SiO_2 on p-type Silicon using THz Spectroscopy," *OSA Annual Meeting, Frontiers in Optics*, FWF1, Tucson, Arizona, 19 October 2005.

Aparajita Bandyopadhyay, Amartya Sengupta, R.B. Barat, D.E. Gary, Z. Michalopoulou and J.F. Federici,

"Application of THz Imaging in Security Screening," *OSA Annual Meeting, Frontiers in Optics*, JWA1, Tucson, AZ, 19 October 2005.

Amartya Sengupta, Aparajita Bandyopadhyay, J.F. Federici and N.M. Ravindra,

"Far-infrared Studies of Silicon related Structures using THz Spectroscopy", *Proc. MS&T 2005, The Physics and Materials Challenges for Integrated Optics: A step in the future for Photonics Devices,* 39, 2005.

Hakan Altan, Amartya Sengupta, J.F. Federici, H. Grebel and D. Pham,

"Estimation of Defect Characteristics of HfO_2 and SiO_2 on p-type Silicon wafers using THz spectroscopy," *J. Appl. Phys,* (under review), 2005.

Amartya Sengupta, Aparajita Bandyopadhyay, R.B. Barat, D.E. Gary and J.F. Federici,

"Study of Morphological Effects on THz Spectra using Ammonium Nitrate," *OSA Topical Meeting, Optical THz Science and Technology*, ME6, Orlando, Florida, 14 March 2005.

When I read, I forget; when I write, I remember; when I do, I understand

-- Anonymous

ACKNOWLEDGMENT

My heart felt thanks go to a great number of people who have made this doctoral dissertation work an exceptionally memorable and rewarding experience.

I particularly want to thank my advisor, Dr John Federici for introducing me to the world of THz spectroscopy and for his encouragement and diligent review of my study and the publications that were inherent in the development of this dissertation. On the same note, I also want to thank Dr. Robert Barat, Dr. Dale Gary, Dr. Richard Mendelsohn, Dr. Nuggehalli Ravindra and Dr. Pradyumna Swain who were kind enough to actively participate in my dissertation committee providing constructive criticisms and valuable suggestions at all stages of this work.

I wish to acknowledge the immense help that I received from Daniel Pham of Sematech Inc. and some of the most significant results reported in this dissertation are a result of our fruitful collaboration. Special thanks go to Dr. N. M. Ravindra for providing some of the samples necessary for the purpose of this dissertation.

I gratefully also acknowledge the many funding agencies (TSWG-ED, Dept. of Homeland Security and the US Army Research Office) whose generous grants facilitated this work. Also, I would like to thank the Graduate Student Association-NJIT, Optical Society of America and the Society of Photonics and Instrumentation Engineers for covering my travel expenses to various conferences.

Finally, no words are enough to acknowledge the constant support and encouragement from my family, especially my parents. Thank you. Lastly, a special note of thanks goes to my long time friend, collaborator and my partner in life who stood firm even in times of crises and would always be there with me in my search of truth.

TABLE OF CONTENTS

TABLE OF CONTENTS
(Continued)

TABLE OF CONTENTS
(Continued)

LIST OF TABLES

LIST OF FIGURES

LIST OF FIGURES
(Continued)

LIST OF FIGURES
(Continued)

LIST OF FIGURES
(Continued)

CHAPTER 1

INTRODUCTION

The technology of generating short optical pulses has advanced remarkably in the recent years. The availability of short optical pulses, especially those of femtosecond laser pulses, and the development of semiconductor technology, including the ultrafast photoconductive thin films and semiconductor quantum structures as a fraction of its products, have fostered an innovative field called THz optoelectronics which resulted in the birth of THz time domain spectroscopy[1]. It is a relatively new area of research in the field of material characterization which was first demonstrated in 1988[2]. Recently, this field is undergoing major changes as THz sources and detectors have been developed to a point where reasonable acquisition rates and high signal to noise ratio are achievable[3]. One of the main objectives in this field is to be able to know the effect of the interaction of THz beams with various materials and create a library of the spectroscopic data of different materials which can then be used to develop THz imaging systems and study the dynamic response of novel materials such as nanotubes and artificial dielectrics.

One of the challenges in THz spectroscopy is to develop analytic methods to extract meaningful information from the experimental spectroscopic data. Particularly, the problem of identifying specific materials based on their THz response has far reaching consequences. Some materials have a multitude of absorption lines at room temperature corresponding to THz frequencies, thereby motivating the current work.

In this thesis, an attempt has been made to study different materials of contemporary interest to categorize their spectral signatures. It emphasizes the use of THz radiation as a non-invasive tool to investigate the far infrared response of

semiconductors, high dielectric constant materials and some other materials of contemporary interest. In addition to material characterization, it has been shown that THz radiation can be used effectively to study grain size dependent scattering effects on the extinction spectra of materials.

1.1 Introduction

This chapter introduces the field of THz time domain spectroscopy (THz-TDS) and discusses the motivation of this work for characterization of materials using such techniques. It presents the roadmap for this thesis and a concise summary of the original contribution of this work.

1.1.1 THz Radiation

The THz region of the electromagnetic spectrum, loosely defined by[i] 0.1-10 THz (1 THz = 10^{12} cycles/second) has been the most *under-explored* regions until recent times. THz radiation was discovered by Heinrich Rubens and Ernest Fox Nichols at the University of Berlin in 1896. After Nichols left Berlin, Rubens continued the work, and in 1900 he isolated wavelengths of 6THz (50 microns) after careful measurements.

By its very nature, THz radiation bridges the gap between microwave and optical frequencies. The THz band lies at the border of these two regimes as shown in Figure 1.1 and is somewhat resistant to the measurement techniques employed in these well established neighboring bands.

[i] Some authors define 0.1-30 THz as the THz band. While there is no agreement in the literature, we have adopted 0.1-10THz as it corresponds to the traditional "THz Gap" region.

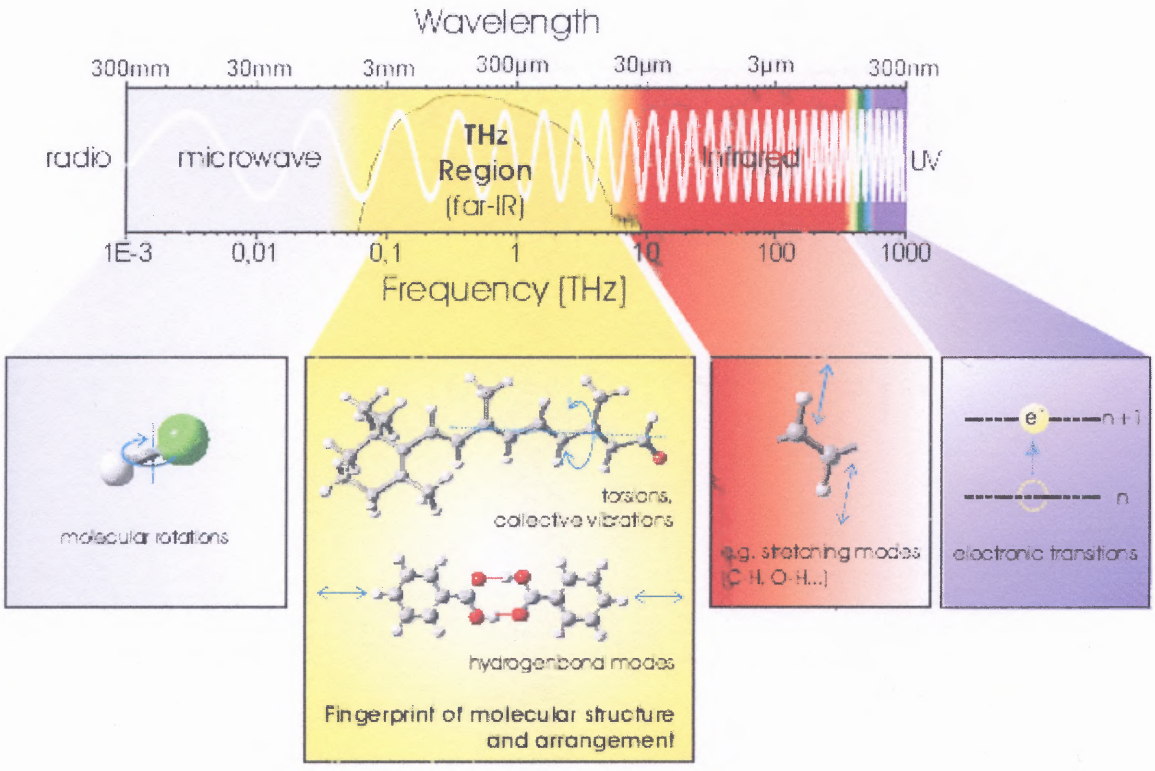

Figure 1.1 The THz "Gap".
(Source: Marcel Stillhart, NLO Kolloquium 2004-2005; THz Waves for Imaging and Spectroscopy.)

Historically, the major domain of THz spectroscopy has been to study the molecular vibrational and rotational resonances in the upper atmosphere since high water vapor absorption in the lower atmosphere constrained early interest and funding in THz science[4]. Since the 1990's however, the THz region of frequencies has been employed to look at a wide variety of materials including ceramics[5], environmental pollutants[6], semiconductors[7] and chemical mixtures[8]. THz radiation is now available in both CW and pulsed forms, down to single cycles or less with peak powers upto 10 MW. Novel sources are leading to new science in many areas, as researchers are becoming aware of the opportunities for research progress in their fields using THz radiation. Applications of THz spectroscopy and imaging in such diverse areas as ferroelectrics[9], semiconductor nanostructures[10], photonic crystals[11, 12], superconductors[13, 14], medical diagnostics,

detection and identification of drugs in mail[15], spectroscopy of biomaterials[16] and detection of explosives[17] have been reported.

1.2 THz Spectroscopy Systems

A number of different methods exist for spectroscopic studies in the THz region of frequencies. The most common among them is Fourier Transform Infrared (FTIR) Spectroscopy which has an extremely high bandwidth that enables characterization of material properties from THz frequencies well into the infrared region of the electromagnetic spectrum. In such a spectroscopic system, the sample is illuminated with a broadband thermal source and is placed in one arm of an optical interferometer system and then the arms are scanned with respect to each other. Bolometers are usually used to measure the interferometric output. A Fourier transform then yields the power spectral density of the material. The main disadvantage is its limited spectral resolution and the loss of the phase information.

Higher resolution spectral measurements maybe made using a narrowband system utilizing a tunable THz source or detector. In these systems, the source or detector is tuned across the desired bandwidth and the spectral response of the sample is measured directly. Both FTIR spectroscopy and narrowband spectroscopy are widely used for passive measurements of thermal emission lines of molecules[18].

THz-TDS on the other hand, uses short pulses of broadband THz radiation which are generated by using an ultrafast laser pulse. This technique grew from the pioneering work in the 1980's at AT&T Bell Laboratories and the IBM T. J. Watson Research Center[19, 20]. Though the spectral range in THz-TDS systems is much lower than for FTIR

spectroscopy systems[21], it has a number of advantages that has given rise to specific applications. Most importantly, in THz-TDS, the electric field amplitude is measured in a coherent manner, which results in very high sensitivity and also yields information about the phase. This has an important consequence in the fact that the optical parameters of the material under study can be inferred without using the Kramers-Kronig relations. Figure 1.2 shows the block diagram of a typical THz time domain spectroscopy system.

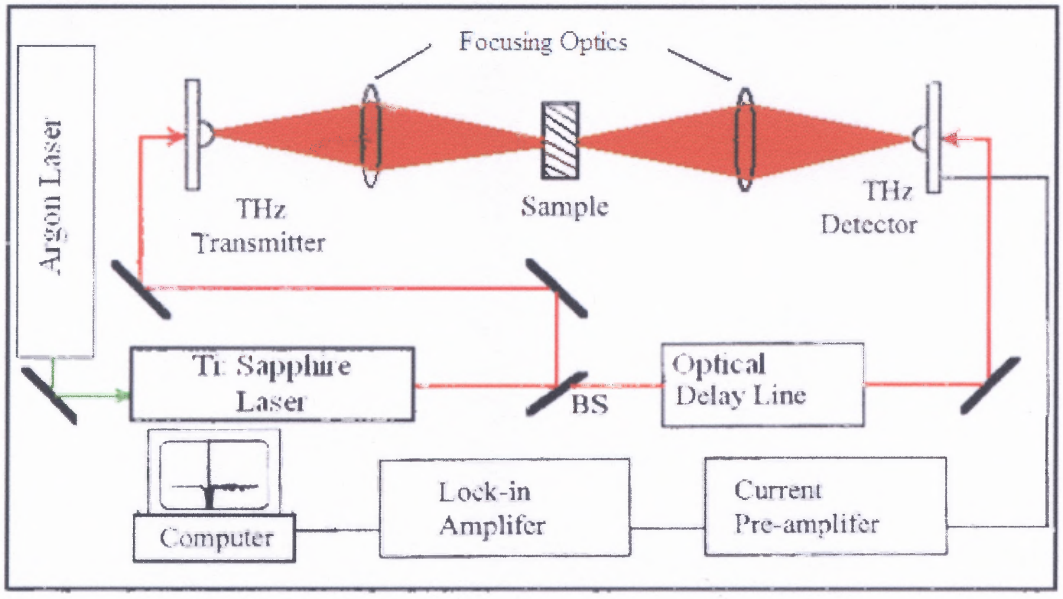

Figure 1.2 Block Diagram of a THz time domain spectrometer.

1.3 Motivation

THz radiation with a fundamental period of around 1 ps, is uniquely suited to study a variety of important systems. For example, electrons in highly excited atomic Rydberg states which orbit at THz frequencies and also, quite a few molecules have rotational states corresponding to the THz region[22]. Biologically important collective modes causes proteins and polar liquids (such as water) to absorb at THz frequencies[23]. Free electrons in semiconductors and nanostructures resonate at THz frequencies[24, 25]. An electron in

Intel's THz transistor races under the gate in ~ 1 ps which corresponds to 1 THz. Gaseous and solid state plasmas oscillate at THz frequencies. Also, scattering effects contribute appreciably to the extinction spectrum of materials when the size of the particles becomes comparable to the size of the wavelengths (1 THz = 300 μm)[26].

At the same time, THz sensing and imaging techniques have several advantages over other sensing and imaging techniques. While microwave and X-ray imaging modalities provide pictures which have depth resolution, THz imaging techniques can provide depth as well as spectral information. The unique rotational and vibrational responses of biological materials within the THz range provide information that is generally absent in optical, X-ray and NMR images. Additionally, THz radiation easily penetrates inside many dielectrics which are opaque to visible light making them a useful and complementary imaging source in this context.

1.4 Dissertation Overview

The aim of this research has been to use THz radiation to characterize materials that are of current interest to the scientific community. The research involved optical spectroscopy system design, assembling the requisite hardware and the development of computational algorithms for the analysis of experimental data to characterize different materials. Numerous ideas have been brought together and unified in their potential for the advancement of THz spectroscopic studies.

The choice of the materials for characterization using THz spectroscopic techniques was based on the relative impact factor of the materials for industrial applications and their characterization using THz time domain techniques. Figure 1.3

shows the current relative impact factor (based on the number of papers) of the materials that have been investigated as a part of this dissertation. The chapters have also been arranged accordingly.

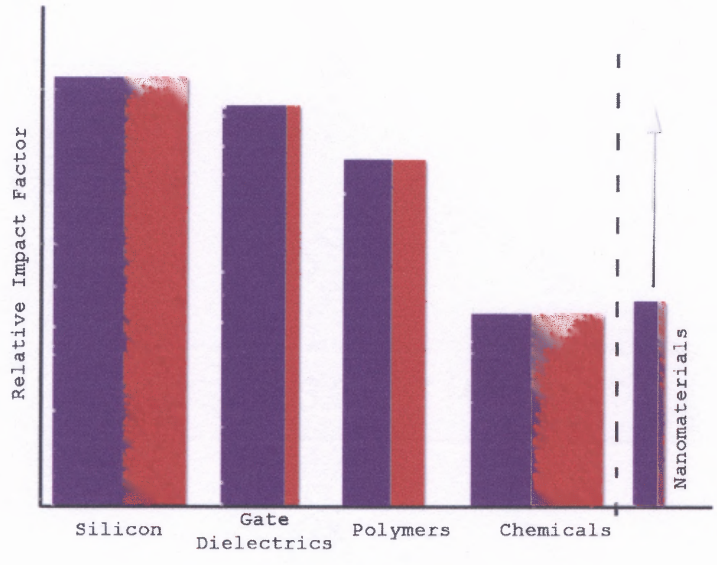

Figure 1.3 Relative Impact Factor of materials for current industrial applications. The red region of each material shows the extent of THz studies with the materials while the magenta region depicts the research of other optical or electrical measurements.

In the current chapter, the introduction and motivation of this dissertation is outlined and the current state of knowledge is summarized. The major contributions of this thesis towards the field of THz science are highlighted. Chapter 2 presents a description of the concept of THz spectroscopy in detail. It introduces the different THz generation and detection techniques currently employed by researchers with special emphasis on the experimental set-ups that were designed for this thesis. The technical specifications of the hardware that was used for the experiments have also been outlined.

Chapter 3 deals with the study of semiconductor materials using THz radiation. This chapter describes a case study of Silicon (since it is a well studied material) and introduces the computational algorithm that was developed to numerically correct for

Fabry-Perot effects in the frequency dependent refractive index of a material and was later used to analyze the experimental data obtained by studying other materials as part of this dissertation.

Chapter 4 is devoted to illustrating the use of THz spectroscopic methods to estimate the interfacial defect density in films of gate dielectric materials deposited on Silicon substrates in which the experimentally obtained results were analyzed using the Drude model.

Chapter 5 deals with the investigation of polymers and chemicals using THz spectroscopic techniques. The first part deals with the study of Ammonium Nitrate with different grain sizes and the second part describes the investigation of a chemical agent of contemporary interest which shows that THz spectroscopic techniques can be effectively used for automated detection of these agents in security screening. In particular, the last part of the chapter describes the study of cyclic olefin polymers, a polymer that is used to fabricate omnidirectional photonic crystal fibers.

The important conclusions and future directions of this work have been summarized in Chapter 6.

1.5 Original Contributions

This dissertation makes a number of significant contributions in the field of THz science and technology. In the area of material characterization, Chapter 3 presents a unique numerical technique to account for the multiple reflection oscillations in the frequency dependent complex refractive index. It also highlights some experimental results which

show that THz radiation can be used to monitor surface roughness of semiconductor wafers.

Chapter 4 details the demonstration of a non-contact characterization method using THz spectroscopy which has been proposed for estimating defect density for industry grade wafers in which high dielectric constant materials are present. Here, the Drude model has been used to analyze the differential transmission experimental results. The contribution of this chapter has been to simultaneously estimate the carrier scattering times and the interfacial defect density and incorporate diffusion effects and an effective medium approximation in the model to account for the dissipation of optical energy within the wafers.

A demonstration of reflection spectroscopy using THz radiation has been described in Chapter 5 and an introductory idea of the theoretical models using Mie theory to predict the effect of grain size dependent scattering effects of THz radiation has also been given. The reflectance spectra obtained have been successively used to develop an interferometric imaging array in parallel research efforts within the group. Also, in this chapter, a cyclic olefin polymer has been studied for the first time using THz techniques and its applications in fabricating THz optics have been discussed.

These contributions will advance the research in THz spectroscopic related areas and provide substantial improvements to the existing knowledge and technology as also serve to extend THz applications to new ground breaking realms.

CHAPTER 2

REVIEW OF THZ TIME DOMAIN SPECTROSCOPY

This chapter sets the perspective for this thesis by providing a historical background of the rich science in THz technology. It reviews the various generation and detection methods of THz radiation which have resulted due to the commercial availability of ultrafast lasers. Also, in recent years there have been significant advances as efficient THz sources and more sensitive detectors have opened up a range of potential applications. Finally, it describes in detail, the theoretical background of the experimental set-up that was built to conduct the experiments described in the later chapters of this thesis.

2.1 THz Sources

Modern THz systems are limited by the lack of availability of high power, low cost and portable sources of THz radiation. Therefore at present, greater part of the scientific research is devoted to develop new sources of THz radiation using novel lasers, high speed electronics and new materials.

THz sources can be broadly classified as incoherent thermal sources, broadband pulsed technologies or narrowband continuous wave (CW) methods.

2.1.1 Broadband THz Sources

The vast majority of pulsed broadband sources of THz radiation operate on the basis of excitation of different materials with ultrafast pulses of laser light. Quite a few different mechanisms are exploited to generate THz radiation which includes photocarrier

acceleration in biased photoconducting semiconductors[27], second order nonlinear effects in electro optic crystals[28], plasma oscillations[29], nonlinear transmission lines[30], and nonlinear processes in fibers[31]. Typical conversion efficiencies of all the above processes are very low (~ 10^{-6}) and consequently, while the average optical power of the ultrafast laser is in the region of few watts, the THz power tends to be in the nW to μW range.

Optical rectification and photoconduction are two of the most common methods for generation of THz pulses. The former is based on the inverse process of the electro-optic effect and the energy of the THz pulse comes directly from the laser pulse excitation. The conversion efficiency depends on the second order nonlinear coefficient of the material as also the phase matching conditions. The pump pulses produce an ultrafast transient polarization, *P(t),* which radiates at THz frequencies. The temporal profile of the THz pulse is given by the second time derivative of the transient polarization[32]. Much of the research nowadays is focused on optimizing the THz generation through investigation of material properties of electro optic crystals which include conventional semiconductors such as GaAs and ZnTe[33], organic polymers like DAST[34] and many others. It should be remembered however, that optical rectification produces THz pulses of low power but has the advantage of providing high bandwidth which might extend upto 50 THz[35].

The photoconductive approach uses high speed photoconductors as transient current sources for radiating antennas[36]. Typical photoconductors include low temperature grown GaAs (LTG-GaAs), InP and radiation damaged Silicon on Sapphire (SOS). Metallic electrodes are used to bias the photoconductive gap and form the

antenna. Details about this mechanism will be outlined in Section 3 where the experimental set-up built for the purpose of this dissertation will be described.

2.1.2 Narrowband THz Sources

Sources of narrowband THz radiation are generally used to achieve very high resolution in spectroscopic studies. They also have potential applications in telecommunications and are particularly attractive for inter satellite links offering high bandwidth. A number of techniques are under development, some of which are upconversion of electronic RF sources, lasers and backward wave oscillators[37, 38, 39].

The most common technique for generating low power CW THz radiation is microwave generation followed by frequency multiplication which has been possible due to the commercial availability of compact all-solid-state devices. Tuning bandwidths are typically 5-10% for highest power devices. Power ranges from 30 mW near 0.2 THz to about 1 μW at 1.6 THz. Utilizing such methods, frequencies as high as 2.7 THz have been demonstrated[40]. Research also continues to increase the frequency of GUNN and IMPATT diodes to the lower reaches of the THz region using alternate semiconducting structures and improved fabrication techniques[41].

Backward wave oscillators that are available commercially have powers varying from 100 mW near 0.1 THz to 1 mW near 1.2 THz. However, current designs only give multimode THz beams as the output.

Gas lasers are another common source of THz radiation. In these sources, a CO_2 laser pumps a low pressure gas cavity which lases at the emission frequencies of the gas molecules. These lasers are spot tunable and typically require very large cavities and KW power supplies; however they can provide high output powers – power levels upto 1 W at

2.5 THz have been demonstrated in the laboratory. Methanol and HCN lasers are most popular and they are in common use for spectroscopy and heterodyne receivers[42, 43].

Extremely high power THz emissions have been achieved using free electron lasers (FEL) with energy recovering linear accelerators[44]. FELs use a high velocity bunch of electrons propagating in vacuum through a strong, spatially varying magnetic field. The magnetic field causes the electrons to oscillate and emit photons. Mirrors are used to confine the beams to the electron beam line, which forms the gain medium of the laser. Even though such systems impose size constraints and require a dedicated facility, they may operate in either CW or pulsed mode and provide average brightness about six orders of magnitude higher than typical photoconductive antenna emitters.

Some optical techniques have also been pursued to generate narrowband THz radiation. In one such approach, two CW lasers with slightly differing central frequencies are combined in a material exhibiting a high second order non linearity such as DAST. The laser frequencies interfere in the material to result in difference frequencies that lie in the THz range[45]. Recent approaches include the mixing of two frequency offset lasers in LTG-GaAs[46].

A very recent technique involves the use of quantum cascade lasers to generate CW THz radiation. Though initial demonstrations involved operation around 10 K[47], recent progress has resulted in CW lasing above liquid nitrogen temperatures at 93 K[48] and pulsed operation at upto 137 K[49].

2.2 THz Detectors

Complementary to the effort of finding new and efficient THz sources, THz detectors are equally the object of active pursuit in the field of THz science. It is quite a difficult task since the power of emitted THz signals is weak. Moreover, due to low photon energies of the THz band (1-10 meV) ambient thermal noise prevails over the THz signal which necessitates the need for highly sensitive detection methods.

2.2.1 Field Detectors

For the detection of the electric field of the THz pulse in THz-TDS systems, a coherent system of detection is employed. Such systems are based on either the method of free space electro-optic sampling (FSEOS) or photoconductive sampling, both of which rely on ultrafast lasers.

In FSEOS, when an electro-optic crystal is put in the THz field, its index ellipsoid is modified by the incident THz pulse and this modification is read by the optical probe beam which changes the state of polarization of the optical beam. The polarization state is detected by a pair of balanced detectors. Figure 2.1 shows the schematic of the balanced detection scheme. The ellipticity modulation of the optical beam is then polarization analyzed to obtain the information about the amplitude and phase of the THz pulse. It has been found that <110> oriented zinc blende crystals provide the highest sensitivity. ZnTe is a popular crystal for electro-optic detection because of its high electro-optic coefficient and mechanical properties though several other crystals have shown promise which include GaSe, $LaTiO_3$ and DAST[50, 51]. Extremely high detection bandwidths in excess of 100 THz have been demonstrated using thin crystals and very short pulses of laser light[52].

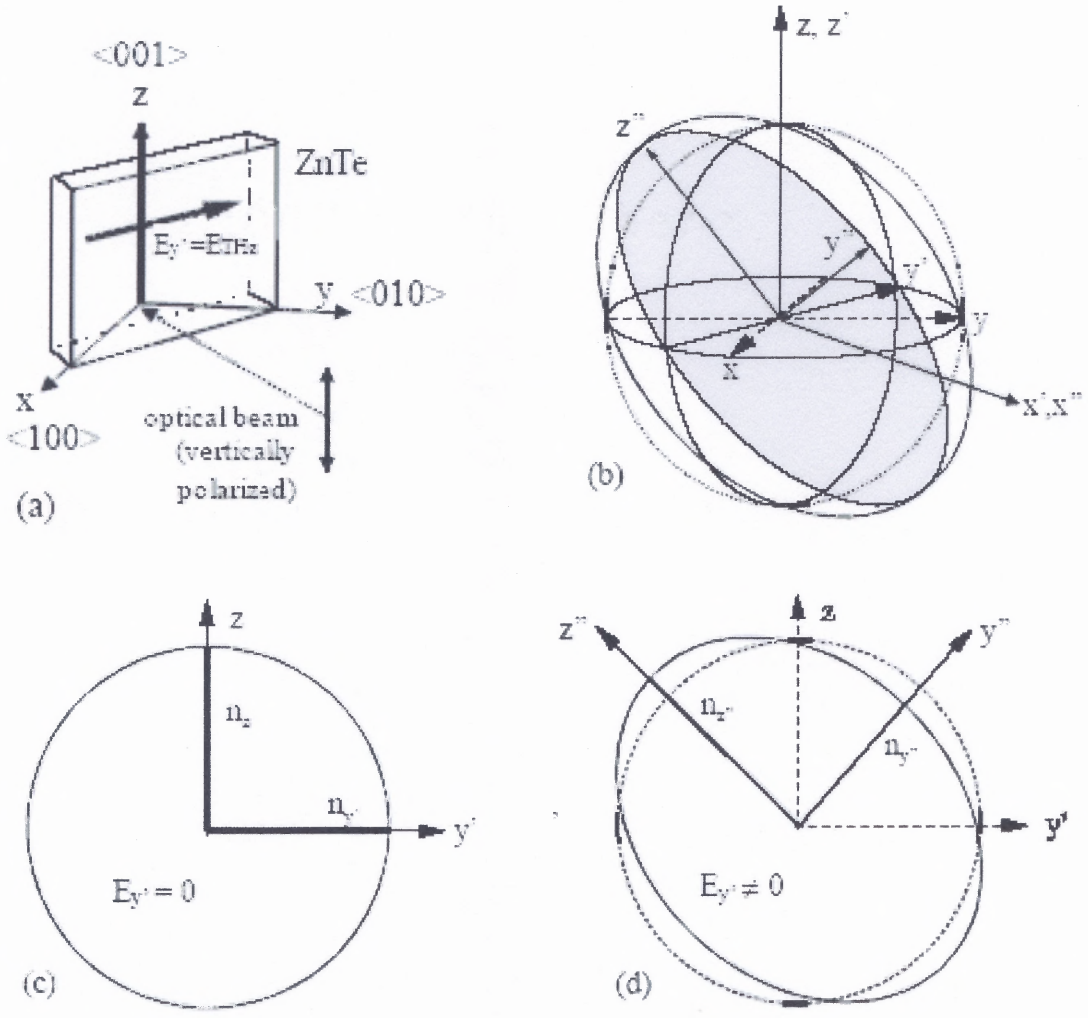

Figure 2.1 (a) Relative orientations of the THz E field and the polarizations of the THz and laser probe with respect to ZnTe, (b) the primed axes describe the optical and THz probe propagation (x'), the THz (y') and the probe beam (z') polarization. The double primed axes refer to the orientation of the main axes of the refractive index under the applied THz bias, (c) and (d) depicts the projection of the ellipsoid on the surface of the crystal as seen by the laser probe without the THz (c) and with the THz (d).

In the photoconductive sampling method, an unbiased photoswitch is used to measure the THz field. THz-TDS systems based on photoconductive emitters and receivers have been demonstrated with flat spectral responses between 0.3 THz and 7.5 THz[53]. Ultrahigh bandwidth detection has also been demonstrated using photoconductive

sampling techniques with detectable frequencies in excess of 60 THz[54]. Details of this method will be given in Section 3.

Other detection configurations that increase the sensitivity of the detection method involves the procedure of heterodyne detection which consists of mixing of two signals, the incoming THz CW signal and the local oscillator (LO) signal. The downshifted signal is then amplified and measured[55]. However, this method is possible for use only with narrowband CW THz radiation.

2.2.2 Energy Detectors

The most popular THz energy detector is the bolometer which exhibits large bandwidth and sensitivity. Most of them require cooling to reduce the spurious thermal noise. Common systems involve helium-cooled Silicon, Germanium and InSb bolometers. Research in superconductors has resulted in extremely sensitive bolometers based on the change of state of a superconductor such as niobium. A single photon detector for THz photons has also been demonstrated[56] and though detection speeds are currently limited to 1 ms, high speed designs have been proposed and this has the potential for revolutionizing the field of THz detection.

2.3 Basic THz Time Domain Spectroscopic Set-up

The experimental set-up that was built for the purpose of this thesis is based on the photoconductive mode of operation; that is, photoconductive antennas are used both as the source and detector of THz radiation. Such method of detection is also known as photoconductive sampling (PC Sampling). A detailed theory involving this approach is presented in the following sub-sections.

2.3.1 THz Generation Involving Photoconductors

LTG-GaAs is the photoconducting material used as the source of THz radiation. An antenna structure is microlithographically imprinted on its surface. This configuration is typically known as an Auston switch. A silicon lens is mounted above the antenna to collimate the emitted THz radiation. Figure 2.2 shows the configuration of the antenna.

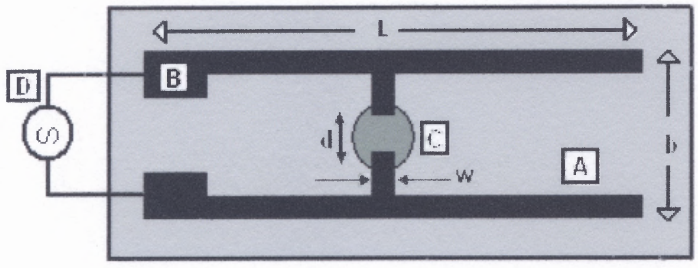

Figure 2.2 Configuration of the Auston switch that has been used in our set-up; A is the LTG-GaAs substrate, B is the transmission line structure, C is the pump laser beam, D is the source of ± 5 V bias at 12 KHz. The values of the switch are L = 1mm, b = 60 μm, d = 10 μm and w = 20 μm.

The physical mechanism for generation of a THz pulse in this configuration begins with an ultrafast pulse with photon energies greater than the band gap of the substrate material. This creates electron hole pairs in the photoconductor which accelerate in the bias field resulting in a transient photocurrent. This fast time varying current radiates electromagnetic waves with THz frequency.

Theoretically, the free carrier lifetime in a photoconductive antenna on LTG-GaAs substrate can be approximated to be equal to the carrier trapping time because the trapping time in mid-gap states is much shorter than the recombination time[57]. Under these conditions, the time dependent behavior of the carrier density is given by,

$$\frac{dn}{dt} = -\frac{n}{\tau_t} + G(t) \qquad (2.1)$$

where n is the carrier density and $G(t) = n_0 \exp(t/\Delta t)^2$ is the generation rate of the carriers due to photoexcitation of the laser pulse with Δt being the pulse width of the laser which in the present case is ~ 100 fs. Table 2.1 shows the variation of the carrier lifetime with the annealing temperature[58].

Table 2.1 Carrier Lifetime in LTG-GaAs for Different Anneal Temperatures

Anneal Temperature, T_a (^oC)	Carrier trapping time, τ_t (fs)
175	280 ± 100
200	375 ± 50
225	450 ± 50
250	660 ± 50
....	....
600	2000 ± 100

The generated carriers are accelerated by the electric field bias with a velocity rate given by,

$$\frac{dv_{e,h}}{dt} = -\frac{v_{e,h}}{\tau_{rel}} + \frac{q_{eff(e,h)}E}{m_{eff(e,h)}} \tag{2.2}$$

where $v_{e,h}$ are the average velocity of the carriers, $q_{e,h}$ is the charge of the electron or hole, τ_{rel} is the momentum relaxation time (30 fs in LTG-GaAs) and E is the local electric field. Taking into account the above expressions and Maxwell's equations, the field of the THz radiation at an angle θ relative to the dipole axis is given by,

$$E_{THz}(t) = \frac{1}{4\pi\varepsilon_0 N^2}\left(\frac{p(t)}{r^3} + \frac{N}{cr^2}\frac{\partial p(t)}{\partial t} + \frac{N^2}{c^2 r}\frac{\partial^2 p(t)}{\partial t^2}\right)\sin\theta \tag{2.3}$$

Here c is the velocity of light, ε_0 is the permittivity of vacuum and N is the refractive index of the material in which the dipole is placed. The on-axis far radiated field far from the dipole is therefore simply described by,

$$E_{THz}(t) \propto \frac{\partial^2 P}{\partial t^2} \propto \left(ev\frac{\partial n}{\partial t} + en\frac{\partial v}{\partial t} \right) \tag{2.4}$$

The first term describes the carrier density charge effect while the second term describes the effect of the application of the electric field bias that is applied to the antenna. The main results can be summarized as,

(a) E_{THz} is proportional to the inverse of the effective mass of the carriers. Since in LTG-GaAs, the effective mass of the holes is five times larger than that of electrons, the effect of the holes is comparatively reduced.

(b) The first term in Equation 2.3 is much greater than the second and so the THz radiation emitted is mainly due to the ultrafast change in carrier density[29].

(c) The pulse width of E_{THz} becomes larger when the width of the laser pulse is increased.

The antenna geometry also plays an important role in the generation of THz radiation and the geometry that exists in the photoconductive switch in the experimental set-up is a dipole broadside antenna which resonates around a frequency of 0.5 THz.

2.3.2 THz Detection Involving PC Sampling

An identical antenna structure like the emitter photoconductive antenna is used. Instead of applying a bias to the photoconductor, a current amplifier coupled with a lock-in amplifier syncronized with the emitter bias frequency is used to measure the transient voltage across the antenna terminals while the photoconductor is biased by the instantaneous THz field. The configuration of the detection scheme is shown in Figure 2.3.

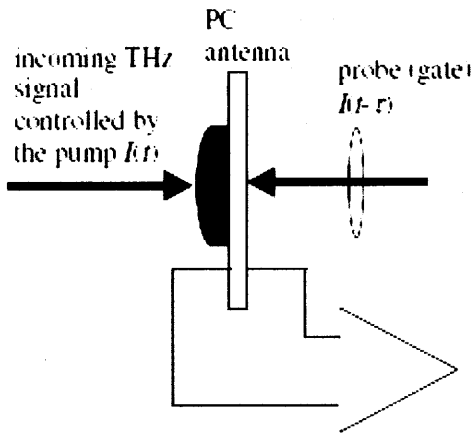

Figure 2.3 Detection configuration for PC Sampling.

In PC Sampling, the reconstructed THz waveforms depend not only on the actual electric field, $E_{THz}(t)$ incident on the receiver antenna but also on the frequency dependent antenna response $H(\omega)$, the carrier lifetime τ_l and the momentum relaxation time τ_{rel}. The charge generated at the terminals of the antenna is given by[59],

$$q(\tau) = \int v(t)g(t-\tau)dt \tag{2.5}$$

where $v(t)$ is the induced bias voltage across the photoconducting gap obtained from,

$$v(t) = \int H(\omega)E(\omega)\exp(i\omega t)d\omega \tag{2.6}$$

and the time dependent conductance $g(t)$ is dependent on the carrier lifetime and momentum relaxation times. Here $E(\omega)$ is the Fourier transform of the incident THz electric field $E_{THz}(t)$, $H(\omega)$ is the transfer function of the antenna, i.e. the ratio between the voltage induced at the antenna terminals and the electric field, both represented in the frequency domain. $H(\omega)$ can be approximated in the current experimental set-up to be $\sim j\omega$ since the dipole is short and it has a silicon lens attached at the back to collect the THz radiation.

2.4 Different THz-TDS Configurations used for Experiments

Figure 2.4 shows a diagram of the basic experimental configuration for THz time domain spectroscopy. Parabolic mirrors were used to collimate and guide the THz beam through the sample to the detector.

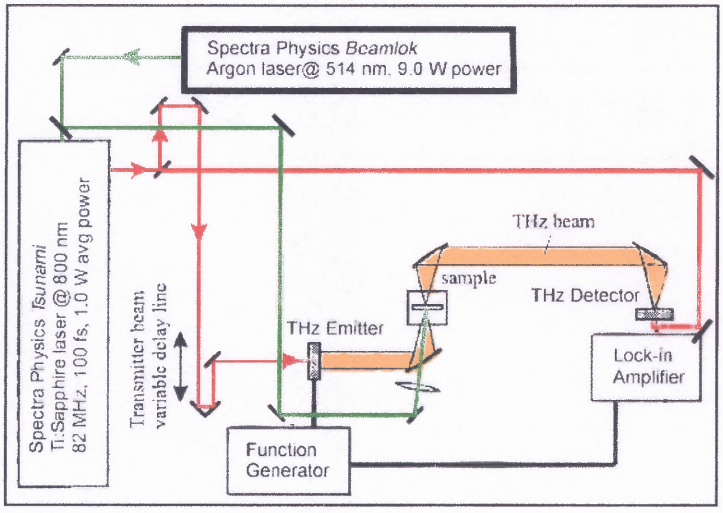

Figure 2.4 THz-TDS experimental set-up.

In most cases, this region was enclosed and purged with dry nitrogen to eliminate the effects of water vapor absorption. The set-up is modified depending on the type of information that needed to be extracted from the experimental time domain data. However, they can be broadly divided into three generic classes.

(a) THz transmission set-up: This set-up had been used for most of the work that will be described later in this thesis. The sample investigated was placed at the focus of the two parabolic mirrors. The spot size of the THz beam is ~2-3 mm.

(b) THz Reflection set-up: In these studies, one of the plane mirrors was either blocked with the sample (if the sample was large to block the entire mirror) or was replaced with the sample. The spot size of the THz beam is ~40 mm in this configuration and so it had to be ensured that both the sample and the mirror have been illuminated with equal amounts of THz radiation and so in the case of smaller samples, the big plane mirrors were replaced with smaller mirrors.

(c) Optical Pump-THz Probe experiments: The arrangement is similar to the transmission geometry except the addition of an optical beam to pump the sample. The optical pump beam and the THz beam were perfectly synchronized

as either both were triggered by the same ultrafast laser or the sample was pumped by CW laser radiation.

The transmission and reflection set-ups have been used for performing equilibrium studies of materials when we wanted to obtain information about the complex refractive index spectrum of the material. The optical pump-THz probe set-up has been used for non equilibrium measurements when the change in response of the sample induced by optical excitation was studied by probing the sample with a THz pulse.

For some experiments in this dissertation, a T-Ray 2000™ system has been used, the schematic of which is shown in Figure 2.5. It consists of fiber pigtailed THz sources and detectors and further details of the system is available here[60].

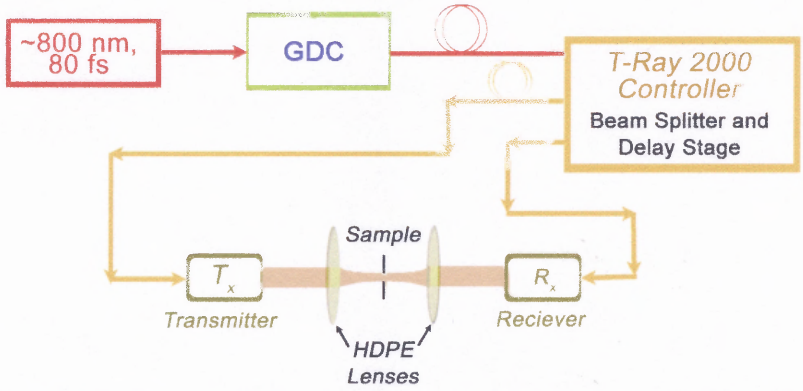

Figure 2.5 The T-Ray System. It consists of a diode pumped solid state laser emitting < 80 fs at 800 nm, a group dispersion compensator (GDC) for shortening the pulse broadening, the T-Ray control Unit which controls the delay stages and the THz transmitter and receiver. The high density polyethylene (HDPE) lenses were introduced to focus the collimated beam onto the sample.

2.5 Technical Specifications of the Hardware

(a) Ultrafast Laser System I: Spectra-Physics® *Tsunami* Ti:Sapphire laser with 1.2 W of power was used which could be tuned to operate between 780 nm and 850 nm. The typical wavelength of operation for most of the experiments was 800 nm. The pulse width of the same varied between 60 fs and 125 fs. This was pumped with 9.0 W of power by a Spectra-Physics® *Beamlok 2080* Argon laser which operated at 514 nm.

(b) Ultrafast Laser System II: A home built Clark MXR® Ti:Sapphire laser was used which gave 0.5 W of power and operated at ~ 800 nm with a pulse width of 150 fs. This was pumped by a Coherent® *Innova 200* Argon Laser operating at 514 nm with 9.0 W of power.

(c) The T-Ray 2000 System: It consists of a diode pumped solid state laser emitting < 80 fs at 800 nm, a group dispersion compensator (GDC) for shortening the pulse broadening, the T-Ray control Unit which controls the delay stages and the THz transmitter and receiver.

(d) Function Generator: Agilent Technologies® Model 33120A function generator was used to bias the emitter photoconductive antenna with a square wave voltage of 5.0 Volts at a frequency of 12 KHz.

(e) Current Amplifier: Ithaco® Model 1211 current preamplifier was used to measure the current produced due to the arrival of the THz waveform at the detector antenna.

(f) Lock-in Amplifier: EG&G® Model 7260 DSP amplifier was used to digitize the signal at the terminals of the detector antenna. The reference frequency was provided from the function generator at the emitter antenna.

(g) Translation Stages: Two Newport® UR73PP motorized linear translation stages were used to perform the experiments. One was used to map out the entire THz waveform and the other was used to control the arrival of the pump pulse with respect to the THz pulse in optical pump – THz probe measurements. The stages provided 200 mm of travel with 1μm resolution and were controlled by Newport-Klinger® motion controller.

(h) THz antennas: High resistivity GaAs wafers had been used to fabricate the antennas. The antennas were fabricated at Lucent Technologies, Murray Hill, NJ and Picometrix, Ann Arbor, MI.

CHAPTER 3

CHARACTERIZATION OF SEMICONDUCTORS

The ultimate goal of all THz systems is to extract information about the sample under investigation. In the current chapter, the frequency dependent optical constants for a semiconductor wafer, namely Silicon, are investigated.

In this work, numerical models based on Fabry-Perot effects have been developed to characterize Silicon wafers by eliminating the effect of multiple reflections within the wafers. Some preliminary interesting results obtained by studying single side polished Silicon wafers have also been reported. The results show significant improvement than previous values that have been quoted in the literature.

3.1 Objective and Motivation

Thin film silicon and related materials are a promising class of materials that have been under development for numerous applications. Such materials have attracted considerable attention owing to their high stability, carrier mobility and doping efficiency making them promising candidates for low cost, efficient and reliable components for the microelectronics industry.

The THz frequency range is particularly interesting for semiconductors as the majority of the oscillator strength of the Drude conductivity falls in this region[61, 62, 63]. This is important, as it allows non-contact characterization of the properties of semiconductors like index of refraction, absorption coefficient, real and imaginary parts of the dielectric constant and doping concentrations which is necessary for their

applications in nanoelectronics where it is difficult, if not impossible, to use conventional probes. The interaction of free carriers with photons in the THz or the far infra-red region is one of the critical concerns for device design at these frequencies.

One of the main motivating factors of this work was to utilize the THz spectroscopic technique on a well studied system like Silicon and developing corresponding analytical models before proceeding to study systems that are not as well characterized. In a comparison of THz-TDS with FTIR spectroscopy measurements[64], even though the latter is superior above 2 THz, the limited power of the radiation sources and problems with the thermal background favor THz-TDS below 2 THz.

Until recently, most of the previous absorption studies of doped Silicon had been limited to the mid infra-red wavelength ($\lambda << 40\mu m$)[65, 66]. However, with the advent of THz science and technology in the past decade or so, there have been leaps and bounds towards studying different materials in this region of the electromagnetic spectrum.

Previous measurements with FTIR spectroscopy extend down to 0.6 THz where the data are relatively imprecise. Recent studies employing THz-TDS techniques have shown that intrinsic Silicon is an exceptionally transparent optical material at THz frequencies[24, 67, 68, 69]. Additionally, there have been quite a few reports of numerical algorithms that have been developed to model the propagation of THz radiation using the Drude approximation and finally extracting the optical parameters of the materials under study[70, 71, 72, 73].

In this work, a generalized numerical method has been proposed to determine the complex index of refraction of materials which may lead to estimation of other related properties of the material such as electrical conductivity. This takes into account the

effect of multiple oscillations within the material being investigated and thus, the model can also be extended to the case when the sample is optically thick (when the transit time of the THz pulse is much larger than the duration of the pulse itself). Various types of silicon wafers have been used to validate the analysis which can be divided into three different classes on the following basis: resistivity, polishing and presence of oxide layer.

The results are very promising from the point of view of semiconductor metrological applications since it has been shown experimentally, that surface roughness on the face of the wafer affects the THz transmission through each side of the wafer. This would enable to distinguish between double side polished and single side polished wafers using a non-contact technique. Additionally, the value of the refractive index obtained from the proposed numerical technique is much closer to the expected values and thus the work attempts to address some of the discrepancies in the values of the refractive index that have been obtained by other researchers[24, 68, 69].

3.2 Experimental Arrangement

A generalized scheme for THz-TDS has already been described in Section 2.4; in Figure 3.1 a detailed schematic has been provided which has been used for experimental measurements for this part of the dissertation.

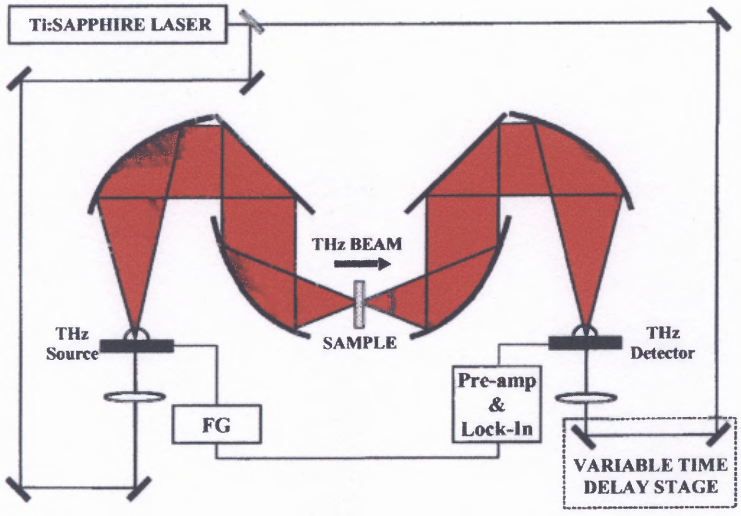

Figure 3.1 Experimental arrangement for linear THz transmission measurements. The THz source and detectors are fabricated on LTG-GaAs, FG is the function generator which is used to bias and modulate the THz source, Pre-amp amplifies and converts the detected current (~nA) to voltage (~200 mV) and the lock-in synchronizes the detector process with the generator so that we have coherent detection. The variable time delay stage is used is used to map out the complete temporal profile of the THz pulse. The typical resolution of the set-up is 30 GHz.

3.3 Samples Studied

Table 3.1 summarizes the different types of wafers that were used in this study. All the wafers were of 4" diameter and were supplied by Virginia Semiconductors Inc and Silicon Sense Inc.

Table 3.1 Parameters of Wafers that were Used in the Experiments

Wafer	Thickness	Resistivity	Polish	Exposed Side
p-type Silicon	50 μm	10-100 Ω-cm	Double side	<100>
p-type Silicon	250 μm	10-100 Ω-cm	Double side	<100>
p-type Silicon	475 μm	1-2 kΩ-cm	Single side	<100>
SiO_2 on Silicon	SiO_2: 0.5 μm Silicon: 700 μm	18-22 Ω-cm	Double side	<100>

3.4 Theoretical Model

The spectroscopic method consists in the measurement of a reference waveform $E_r(t)$ and a sample waveform $E_s(t)$ with the sample placed at the focus of the THz beam as shown in Figure 3.1. The experimental transmission spectrum $\tilde{T}_{exp}(\nu)$ is calculated using the Discrete Fourier Transform (DFT) of the sample and reference measurements as,

$$\tilde{T}_{exp}(\nu) = \frac{\left|E_{sample}(\nu)\right|}{\left|E_{ref}(\nu)\right|} \tag{3.1}$$

In the case of optically thin samples (the transit time of the THz pulse through the sample is comparable to the width of the pulse itself), the overlap between successive echoes limits the ability to break up the transmitted THz signal through the sample into individual echoes and hence, the effects of multiple reflections through the sample have to be considered while developing an analytical model with the following assumptions:

(a) The electromagnetic response of all the media is linear,

(b) The sample has two optically parallel and flat sides and

(c) The sample and the overlayers are isotropic without the presence of any surface charges

The transmitted electric field of the sample $E_s(\nu)$ is given by[74],

$$E_s(\nu) = \left(\prod_{\substack{a,b=1 \\ a \neq b}}^{a,b=m} T_{ab} P_m(\nu, d) \right) \left(\sum_{k=0}^{\infty} \prod_{\substack{a,b=1 \\ a \neq b}}^{a,b=m} \{ R_{ab} P_m^{\,2}(\nu, d) \}^k \right) E(\nu) \tag{3.2}$$

In the above equation, the second term is the Fabry-Perot term arising out of multiple reflections within the thin samples of Silicon, $E(\nu)$ is the electric field of the emitted THz signal, R_{ab}, T_{ab} are the Fresnel reflection and transmission coefficients at the *a-b*

interface, and P_m is the propagation coefficient in medium m over a distance d and is given by,

$$P_a(\nu,d)=\exp\left[-i\frac{\tilde{n}_a\nu d}{c}\right] \tag{3.3}$$

with $\tilde{n}_a(\nu)=n_a(\nu)+i\kappa_a(\nu)$ being the complex refractive index of medium a. Hence the theoretical complex transmission coefficient $\tilde{T}_{th}(\nu)$ taking into account Fabry-Perot effects is given by,

$$\tilde{T}_{th}(\nu,\tilde{n},l)=\frac{\frac{4\tilde{n}}{(\tilde{n}+1)^2}\exp\left[-i\frac{2\pi(\tilde{n}-1)\nu l}{c}\right]}{1-\left(\frac{\tilde{n}-1}{\tilde{n}+1}\right)^2\exp\left[-i\frac{4\pi\tilde{n}\nu l}{c}\right]} \tag{3.4}$$

Equation 3.4 can be written in the following way to show the contribution of the Fabry-Perot effects,

$$\tilde{T}_{th}(\nu,\tilde{n},l)=\rho_{\text{sin}gle}(\nu,\tilde{n},l)\rho_{FP}(\nu,\tilde{n},l)\exp\left[i(\theta_{\text{sin}gle}(\nu,\tilde{n},l)+\theta_{FP}(\nu,\tilde{n},l))\right] \tag{3.5}$$

In order to evaluate the Fabry-Perot contribution, the samples were assumed dispersionless and to have $\kappa << 1$, so that the total complex transmission coefficient can be expressed in terms of the following functions,

$$\left.\begin{aligned}
\rho_{single}(\nu,n,l) &= \frac{4\sqrt{n^2+\kappa^2}}{(n+1)^2+\kappa^2}\exp\left(-\frac{2\pi\kappa\nu l}{c}\right) \\
\theta_{single}(\nu,n,l) &= \frac{2\pi(n-1)l}{c}+\tan^{-1}\left[\frac{\kappa}{n(n+1)+\kappa^2}\right] \\
\rho_{FP}(\nu,n,l) &= \frac{1}{\sqrt{2\left[1-\left(\frac{n-1}{n+1}\right)^2\cos\left(\frac{4\pi\nu nl}{c}\right)\right]}} \\
\theta_{FP}(\nu,n,l) &= \tan^{-1}\left[\frac{\left(\frac{n-1}{n+1}\right)^2\sin\left(\frac{4\pi\nu nl}{c}\right)}{\left(\frac{n-1}{n+1}\right)^2\cos\left(\frac{4\pi\nu nl}{c}\right)-1}\right]
\end{aligned}\right\} \qquad (3.6)$$

In the above equations, n is the index of refraction of the material, κ is the absorption coefficient and l is the thickness of the sample.

The transmission spectrum deconvolution obtained from the Fourier transform of the measured signals as shown in Equation 3.1 is compared with the modeled transfer function of Equation 3.6 using a minimization algorithm which evaluates the sum square error ε^2 defined as, $\varepsilon^2 = (\Delta\rho^2)+(\Delta\theta^2)$ where $\Delta\rho$ and $\Delta\theta$ are the differences in the theoretically predicted values and the experimentally obtained values of the modulus and the argument of the complex transmission function respectively and are given by,

$$\left.\begin{aligned}
\Delta\rho &= \rho_{single}(\nu)\rho_{FP}(\nu) \sim \left|\tilde{T}_{\exp}(\nu)\right| \\
\Delta\theta &= \left\{\theta_{single}(\nu)+\theta_{FP}(\nu)\right\} \sim \arg\left(\tilde{T}_{\exp}(\nu)\right)
\end{aligned}\right\} \qquad (3.7)$$

Minimization of the error gives a set of values of the refractive index, absorption coefficient and length of the material which are the effective optical quantities due to Fabry-Perot effects in the assumed dispersionless medium. Using these values in the single pass model, actual optical parameters namely the spectra of the refractive index and the absorption coefficient of the dispersive medium are obtained as,

$$\left.\begin{aligned} n(\nu) &= \left[1 - \frac{c}{2\pi\nu l}\arg\left(\tilde{T}_{\text{single}}(\nu)\right)\right] \\ \kappa(\nu) &= \frac{c}{2\pi\nu l}\ln\left[\frac{[n(\nu)+1]^2}{4n(\nu)}\left|\tilde{T}_{\text{single}}(\nu)\right|\right] \end{aligned}\right\} \tag{3.8}$$

The above quantities are the numerically extracted optical parameters for the dispersive thin sample. From the above set of $n(\nu)$ and $\kappa(\nu)$, the real and imaginary parts of the dielectric constant of the material are calculated as functions of frequency[75].

3.5 Results

3.5.1 Demonstration of Reciprocity Principle of Light

The time domain transmission measurements and the corresponding frequency domain spectra for all the double side polished (DSP) wafers under study of thickness 50 μm, 250 μm and 700 μm, demonstrate the reciprocity principle. That is, the two opposite faces of the wafers yield identical transmission spectra under THz illumination. This is very important to assert the fact that THz radiation can be used for semiconductor metrological applications. Figures 3.2 (a) and 3.2 (b) show the experimental time domain plots and the corresponding transmittance for both sides of the 250 μm thick silicon wafer. The transmittance has been obtained by normalizing the DFT of the data of the sample to that of air as given by Equation 3.1.

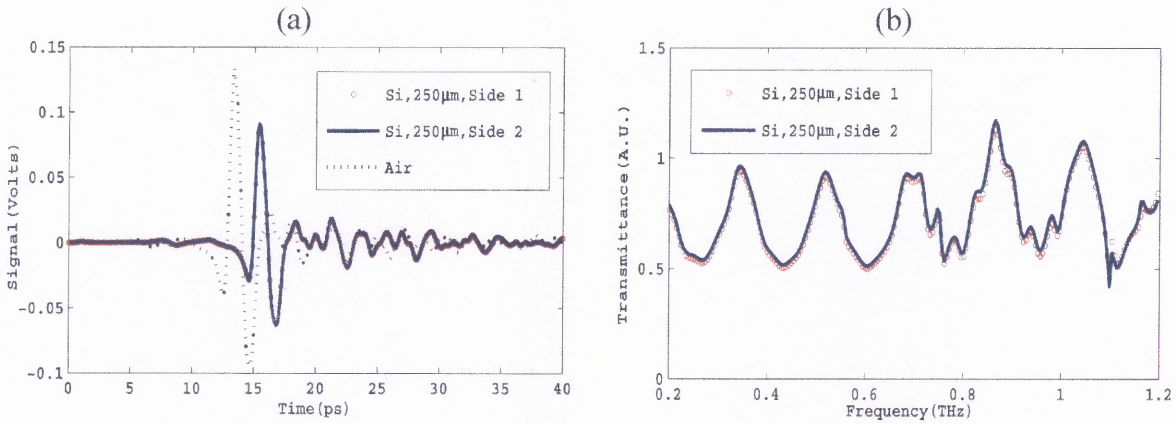

Figure 3.2 Plot of measured THz signal in (a) time domain and (b) corresponding frequency spectrum of a DSP 250 µm p-type Silicon wafer. It is seen that the spectra of the transmitted THz pulse is identical irrespective of the side of illumination.

However as shown in Figure 3.3, when the THz spectrum of the 475 µm thick single side polished Silicon wafer is observed, it is found that the result does not conform to the reciprocity principle. This difference in the spectra from the two opposite faces suggests that probably THz radiation is sensitive to surface roughness and opens up further avenues for the application of THz spectroscopy in estimation of the surface roughness.

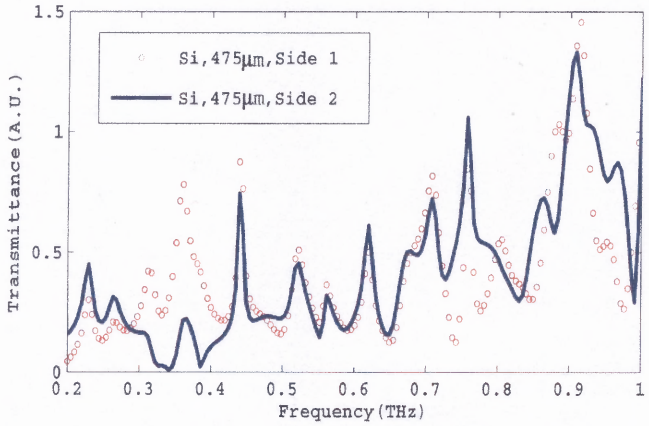

Figure 3.3 THz spectra of single side polished 475 µm thick Silicon wafer. It is seen that the spectra of the two sides are not identical.

3.5.2 Estimation of Refractive Index and Extinction Coefficient Spectra

Using the analysis described in Section 3.1.5, both the real and the imaginary parts of the complex refractive indices as a function of frequency are determined for the silicon wafers using Equation 3.8. Figure 3.4 (a) shows a comparison of the experimentally obtained and numerically extracted frequency dependent refractive indices for the 250 μm thick DSP silicon wafer. The experimentally obtained refractive indices show the characteristic Fabry-Perot oscillations while the numerically corrected value of refractive indices has monotonic variation of about 10% over the frequency range of 0.2 to 1.2 THz.

Figure 3.4 (b) shows the corresponding comparison of extinction coefficient for the same wafer. The absorption is mainly due to the presence of free carriers in the doped wafers[76]. In fact, for a very lightly doped wafer, or conversely, for a semiconductor of high resistivity, THz absorption would be almost negligible. Understandably, apparatus manufactured from high resistivity Silicon are the ones which are extensively used as optical components at THz frequencies.

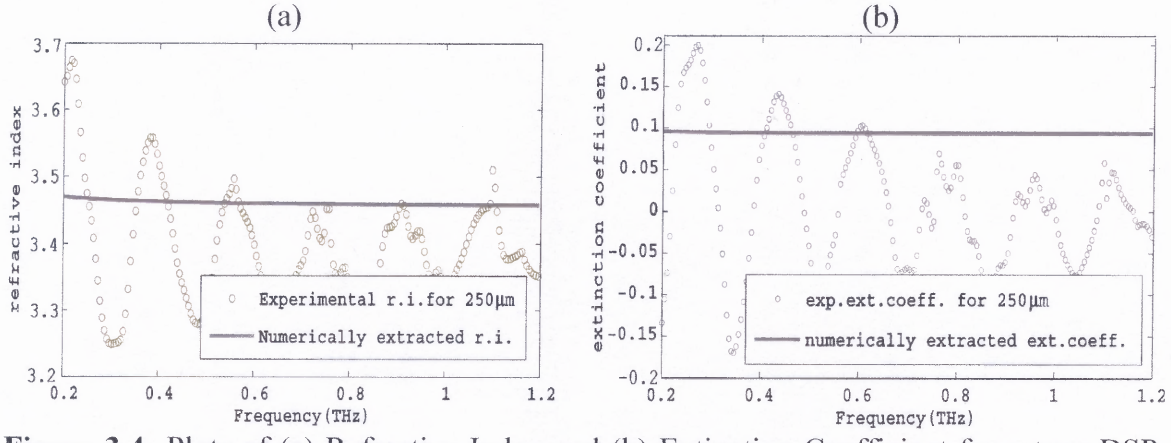

Figure 3.4 Plots of (a) Refractive Index and (b) Extinction Coefficient for p-type DSP Silicon wafers of thickness 250 μm. it is seen that the numerically corrected refractive index is close to the expected value, given by $\sqrt{\varepsilon^{Si}}_0 = 3.42$.

In previously published reports in the literature[61, 67, 68], the variations observed in the index of refraction have been much larger compared to results in the present study which is more reasonable and in accordance with theoretical predictions[77]. The apparent discrepancies cannot be attributed to the difference in resistivity of the silicon wafers and hence, is probably due to the new approach of applying an unconstrained nonlinear optimization technique to account for the effects of multiple reflections within the wafers. Corresponding plots have been shown in Figure 3.5.

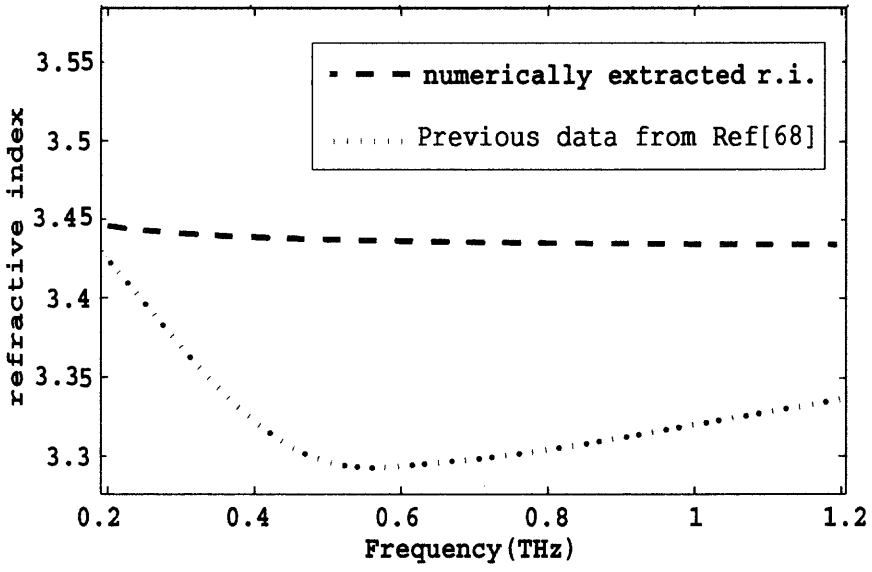

Figure 3.5 Comparison graphs showing the results of the current study and previously published work. The graph of Ref [68] has been digitized from the actual reported data.

3.5.3 Calculation of the Dielectric Constant and Conductivity

Subsequently, the real and imaginary parts of the complex dielectric constants are calculated, the results of which are shown in Figures 3.6 (a) and (b) respectively. It is seen that, they agree well with the theoretical predictions.

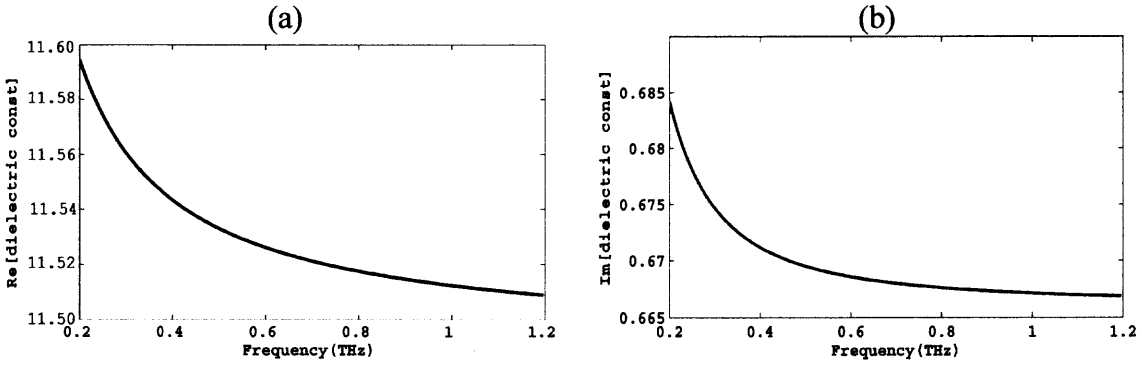

Figure 3.6 (a) Real and (b) Imaginary parts of the dielectric constant of Silicon extracted numerically for the 250 μm thick wafer.

The imaginary part of the complex dielectric constant is directly related to the ac conductivity[78]. The frequency dependent electrical conductivity of the sample is shown in Figure 3.7. The value of the conductivity at the lowest frequency, that is, at 0.2 THz gives an estimation of the dc conductivity, which corresponds to a resistivity of 2 Ω-cm. This is in accord with an independent four probe measurement of resistivity on the same wafer which gave the value to be 4.5 Ω-cm.

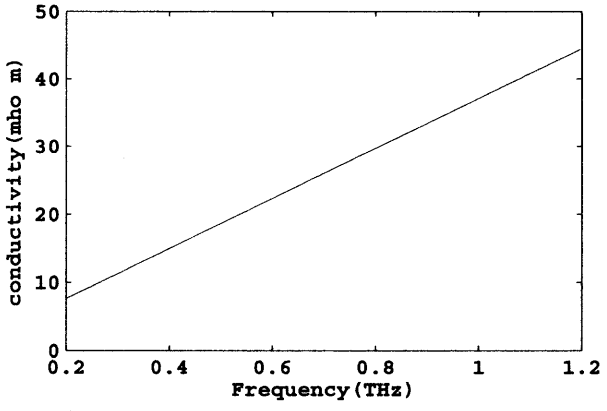

Figure 3.7 AC Conductivity of the 250 μm thick DSP Silicon wafer.

3.6 Conclusions

A unique numerical method to calculate the optical and electrical parameters of unknown homogeneous samples with THz-TDS has been discussed. The advantage of the proposed numerical technique is that it requires knowledge of only the primary transmission and the number of echoes recorded for optically thick samples and only the primary transmission for thin samples. Additionally, the method uses the simplex algorithmic approach to minimize the errors between the experimental and theoretical values and results in the actual optical constants of the sample under investigation. The results show a significant improvement in the values of the refractive index and also show that surface roughness has an effect on the THz transmission.

CHAPTER 4

CHARACTERIZATION OF GATE DIELECTRIC MATERIALS

In this chapter, the results of the investigation of some gate dielectrics, namely Silicon Dioxide (SiO_2) and Hafnium Dioxide (HfO_2) with THz radiation is discussed. A brief overview of the various absorption processes in materials is also presented with special emphasis on the absorption mechanisms of our interest due to the current investigation. The analysis involves the method of impedance matching incorporating diffusive effects and an effective medium approximation which have been used to develop a model to fit the experimental data, subsequently estimating the number of defect states in the interfacial layer between the gate dielectric and p+ Silicon layer. The results are noteworthy in terms of its applications to the microelectronics industry whereby a non-contact technique in the form of THz radiation might be an alternative to the conventional contact techniques that are used to characterize gate dielectrics.

4.1 Introduction and Motivation

For a long time, silicon based dielectrics (SiO_2, Si_3N_4, SiO_xN_y) have been widely used as the key dielectrics in the manufacture of silicon integrated circuits and all other semiconductor devices. Continual scaling of devices has led to reduction in dimensions with an increased performance and a decrease in the cost of devices. These phenomenal trends are popularly quantified as "Moore's law" which predicts that number of components per chip doubles every eighteen months[79] and as Figure 4.1 shows, Moore's law has been followed for a surprisingly long time. This continued scaling of

complimentary metal-oxide-semiconductor (CMOS) integrated circuit technology is critical for the silicon based microelectronics industry and is pushing the Si-SiO_2 system to its very limits, thereby leading to the consideration of alternate gate dielectrics to replace Silicon dioxide[80, 81].

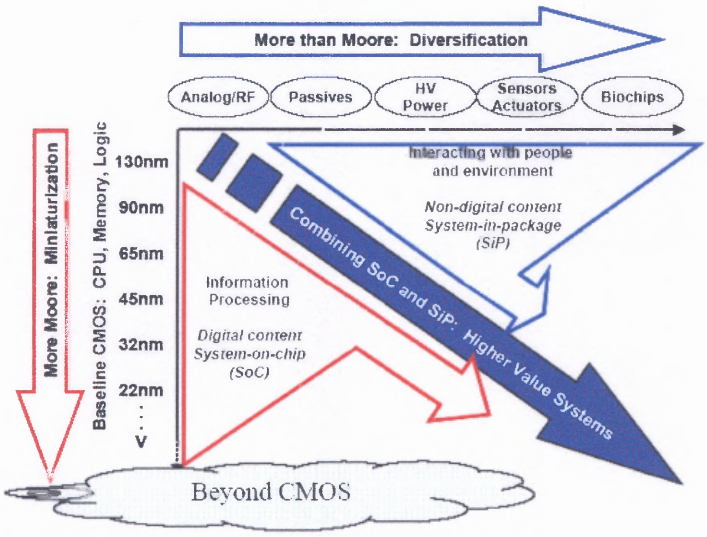

Figure 4.1 Moore's Law and more.
(Source: 2005 International Technology Roadmap for Semiconductors)

A fundamental nature of silicon technology is the fortuitous nature of silicon as a material -- it can be reacted with oxygen or nitrogen in a controlled manner to form superb insulators with excellent mechanical, electrical and dielectric properties. These dielectrics in turn, are used as core components of the two device types that represent the heart of the silicon semiconductor industry: as the capacitor dielectrics used for information storage in dynamic random access memories (DRAMs) and as the transistor gate dielectric in CMOS field effect transistor (FET) logic devices. In both cases, the thickness of the present dielectric, namely SiO_2 or a Si-O-N analogue is becoming sufficiently thin that leakage currents arising from electron tunneling through the dielectrics are posing a problem and are viewed as a major technical barrier[82]. Although

the exact thickness limits are currently the source of much research and debate, one solution of the problem is the replacement of SiO_2 by an alternative insulator with a higher dielectric constant. This implies that the thickness of the dielectric could be increased and one of the most promising candidates being suggested is Hafnium Dioxide[83, 84].

Even though a large number of gate dielectrics have been studied in the past few years, due to its high band gap and adequate conduction band offset[85, 86], Hafnium based high k dielectrics have become a very promising candidate to replace SiO_2 in CMOS technology. If the capacitor dielectric is SiO_2, a capacitance density of 34.5 $fF/\mu m^2$ would correspond to an equivalent oxide thickness t_{eq} of 10 Å. Equivalent oxide thickness represents the theoretical thickness of SiO_2 that would be required to achieve the same capacitance density as the dielectric ignoring issues such as leakage current and reliability. HfO_2 with a bulk relative permittivity of 25[103], therefore affords a physical thickness of 63 Å to obtain t_{eq} of 10 Å. Developing all optical methods involving either linear and/or differential spectroscopic measurements to deduce the effects of this oxide on the Silicon interface is if great interest in the microelectronics industry, specially since it will open up the possibility of online quality monitoring of fabricated microelectronic components.

Additionally, optical pump-THz probe techniques have been very effective in investigating the carrier dynamics of different materials in the THz region of frequencies[87, 88, 89]. Following that approach, in this work, it has been shown that visible pump-THz probe spectroscopic measurements provide an estimation of the number of defect states and the scattering times of the carriers in the interfacial layer between the

dielectric and the substrate. A subsequent Drude analysis incorporating diffusion effects of the photogenerated carriers and an effective medium approximation shows that the defect density for the high dielectric constant material (HfO_2) and Silicon interface is more than at the SiO_2/Si interface which accounts as one of the probable reasons for the decrease in channel mobility under the HfO_2 layer[90].

4.2 Experimental Arrangement

Figure 4.2 shows the schematic of the experimental set-up for performing the optical pump-THz probe measurements. The linear measurements were done using the set-up which has been discussed in Section 3.2. The differential measurements have been obtained by blocking the pump laser beam when taking the linear measurements for the corresponding wafer.

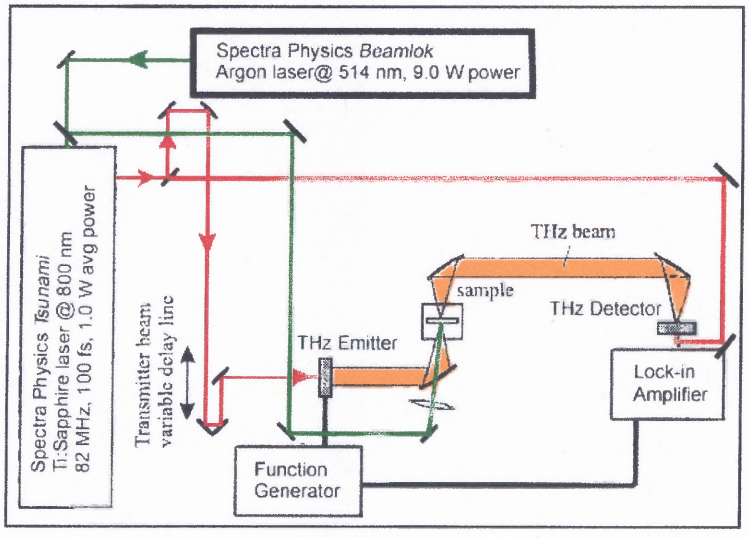

Figure 4.2 Experimental arrangement for pump-probe studies on the gate dielectrics. It was ensured that the pump and the THz beam overlap on the sample and they are incident at almost the same angle. The lens was used to focus the pump beam on the sample; the incident intensity was 0.5 W/cm^2.

4.3 Samples Studied

The wafers provided by Sematech Inc. were 20 cm in diameter and had either a coating of photoresist (PR) or nitride deposition (ND)-Si_3N_4 coating on 70 or 100 Å thick HfO_2 and 50 Å thick SiO_2 dielectric layers. These samples were deposited on a heavily doped p+ layer (Boron doping~10^{18} cm^{-3}, 300 Å thick). Finally there was the p-type Silicon substrate of thickness 500 μm. In addition, different control samples, each coated with either photoresist or Si_3N_4 without any oxide layer was provided. A schematic of the structure of the wafer is shown in Figure 4.3.

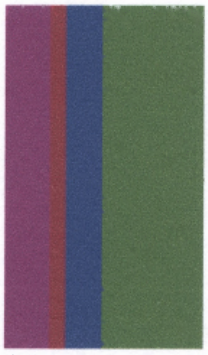

Figure 4.3 Structure of the investigated wafers. p-type Silicon substrate: green, p+ Silicon layer: blue, HfO_2/SiO_2 layer: brown and photoresist/Si_3N_4 coating: magenta.

4.4 Brief Overview of Absorption Processes in Solids

In describing absorption processes in solids, it is possible to categorize the major phenomena under six different sections as shown in Figure 4.4. They can be arranged in the order of decreasing energy transition as:

(i) Electron transition from valence band to higher lying conduction bands: characterized by continuous high absorption processes with structure variations depending on the density of states distributions in the bands involved. The optical absorption constant is usually in the range of 10^5-10^6 cm^{-1}.

(j) Transitions across the band gap of the material: the magnitude and variation of the absorption constant depends on whether the transition involves a photon only (direct transition) or whether it involves both a photon and a phonon (indirect

transition). The absorption constant decreases by many orders of magnitude as the photon energy drops below the band gap energy.

(k) Optical excitations producing a bound electron-hole pair or an exciton: requires less energy than to produce a free electron-hole pair. The exciton can be thought of as a system capable of moving and transporting energy through the crystal without transporting net charge.

(l) Imperfection or impurity absorptions: Presence of imperfections creates energy levels that lie in the region of forbidden gap. Therefore, at energies less than the band gap, it is still possible to excite electrons to the conduction band from imperfection levels occupied by electrons. For very high imperfection densities, the corresponding absorption constant may have values as high as 10^3 cm^{-1}, but in general, is considerably less.

(m)Free carrier absorption: causes a transition to higher energy states within the same band or to higher bands. This process occurs over a wide range of photon energies.

(n) Reststrahlen absorption: absorption of photons in the excitation of optical mode vibrations of the crystal lattice. This does not involve electronic transitions.

The THz range of energies is suitable to study the free carrier absorption effects in materials where, for semiconductors, the absorption has an inverse square dependence on frequency.

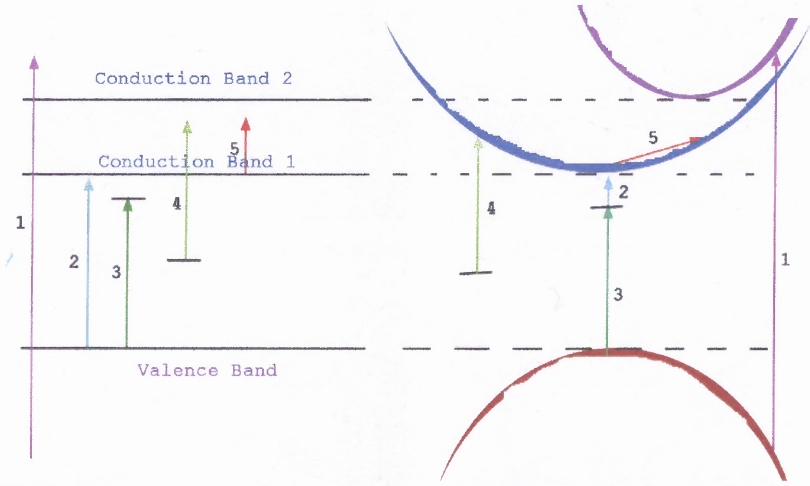

Figure 4.4 Optical transitions shown in the band diagram. (1) excitation from valence band to higher lying conduction band, (2) excitation across band gap, (3) exciton formation, (4) excitation from defects and impurities and (5) free carrier absorption.

4.5 Theoretical Model

The theoretical model is based on the Drude theory which is briefly revisited in Section 4.5.1. The preliminary theoretical model as discussed in Section 4.5.2 neglects any diffusive effects of the pump beam while the advanced analysis incorporating the effects of diffusion and the effective medium approximation has been discussed in Section 4.5.3. Finally, Section 4.5.4 outlines the method for evaluating the number of interface traps in the interfacial layer.

4.5.1 The Drude Model

The Drude model is based on the classical equations of motion of an electron in an optical electric field and gives the simplest theory of optical constants of materials, where the major contribution to the dielectric function is through free carriers. Excellent treatise of the same can be obtained here[91, 92].

This model is not limited to metals (since they have inherent free carriers), even nonconductors show a free electron type behavior at sufficiently high frequencies[93]. Impurities in semiconductors which release either free electrons or free holes, also give rise to optical transitions below the minimum band gap that are characteristic of the Drude theory.

4.5.2 Preliminary Modeling

According to the Drude model, the frequency dependent dielectric constant of a material is given by[61],

$$\tilde{n}^2 = (n+ik)^2 = \varepsilon(\omega) = \varepsilon_\infty - \frac{{\omega_p}^2}{\omega^2 + i\frac{\omega}{\tau}} \tag{4.1}$$

where n is the real and k is the imaginary part of the complex index of refraction, ε_∞ is the dielectric constant of the material at high frequencies, $1/\tau$ is the collision frequency and $\omega_p=(4\pi Ne^2/m_{eff})^{1/2}$, N, e, m_{eff} are the plasma frequency, number density, electronic charge and effective mass of the free carriers (electrons or holes) respectively. Separating the real and imaginary parts of the above equation we obtain,

$$\left.\begin{aligned}\varepsilon_r &= \varepsilon_\infty - \frac{\omega_p^{\,2}}{\omega^2+\frac{1}{\tau^2}}\\ \varepsilon_i &= \frac{\omega_p^{\,2}}{\omega^3\tau+\frac{\omega}{\tau}}\end{aligned}\right\} \qquad (4.2)$$

Two different types of methods can be used for the subsequent analysis of the experimental data. The first is the transfer matrix method and the second is the impedance matching method.

4.5.2.1 Abeles Method of Transfer Matrices. By using the transfer matrix method, the linear transmission at normal incidence through n' layers, n_0 being the first medium is given by,

$$T=\left|\frac{2n_0}{M_{11}n_0+M_{12}n_0n'+M_{21}n_0+M_{22}n_0n'}\right|^2 \qquad (4.3)$$

where $M_{ij}=M_{n+1}M_{n+2}\ldots M_n$, and

$$M_{dielectric}=\begin{pmatrix}\cos\delta_d & \frac{i\sin\delta_d}{n_d}\\ in_d\sin\delta_d & \cos\delta_d\end{pmatrix} \qquad (4.4)$$

where $\delta_d=n_dk_0d_d$ and the symbols have their usual meanings with d_n being the thickness of medium n . Further details following this method of analysis has been worked out elsewhere[94, 95]. However, one of the main drawbacks of this approach is it restricts any

dispersion of the material properties and inherently makes the paraxial assumption of $sin\theta \cong tan\theta \cong \theta$ which is not always true in real-world applications. To overcome such hindrances, the impedance matching approach is considered.

4.5.2.2 Method of Impedance Matching. The impedance of a plane wave traveling in a medium of relative permeability μ_r and dielectric constant ε_r is

$$Z = \sqrt{\frac{\mu_r \mu_0}{\varepsilon_r \varepsilon_0}} = Z_0 \sqrt{\frac{\mu_r}{\varepsilon_r}} \tag{4.5}$$

Since for our case, $\mu_r = 1$, the impedance can be written as $Z = Z_0/n$ where n is the refractive index of the material. When optical radiation is incident on an interface between materials having different impedances, then the amount of optical energy that is transmitted is related to the impedances of all the materials under concern. Since the faces of the wafers under investigation are very flat and parallel, and the light source is coherent, the method of transformed impedances[96] is used to calculate the transmission through such a multilayer structure.

Considering a three layer structure as shown in Figure 4.5 (a), the effective impedances of medium 1, 2 and 3 are[97],

$$\left.\begin{aligned} Z_1' &= Z_1 \cos\theta_1 = Z_0 \cos\theta_1 / n_1 \\ Z_2' &= Z_2 \cos\theta_2 = Z_0 \cos\theta_2 / n_2 \\ Z_3' &= Z_3 \cos\theta_3 = Z_0 \cos\theta_3 / n_3 \end{aligned}\right\} \tag{4.6}$$

It can be shown that the reflection and transmission coefficients of the structure are exactly the same as shown in Figure 4.5 (b) for normal incidence where the effective thickness of layer 2 is given by $d' = d\cos\theta_2$.

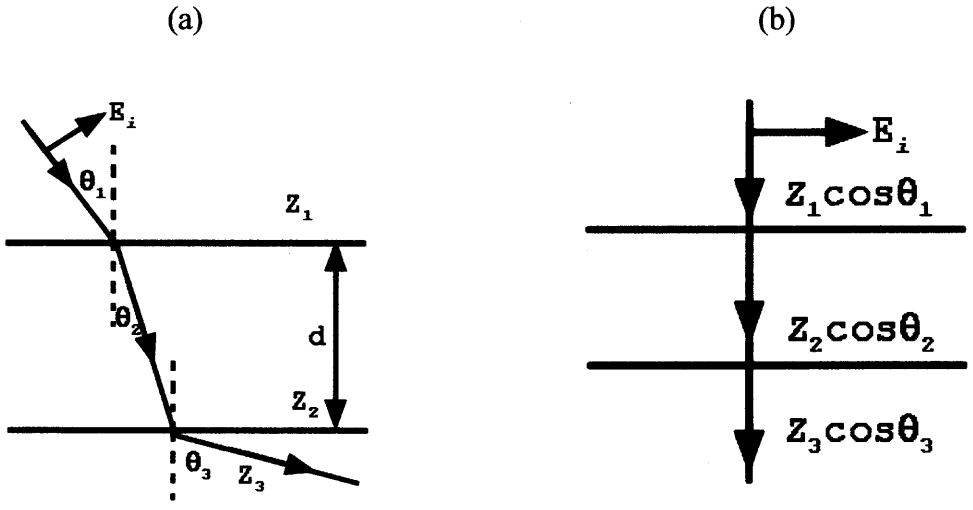

Figure 4.5 Waves passing through a dielectric slab. (a) waves incident at an angle being reflected and refracted and (b) normal impedance structure equivalent to (a).

The transformed impedance of medium 3 at the boundary between media 1 and 2 is,

$$Z_3'' = Z_2'\left(\frac{Z_3'\cos k_2 d' + iZ_2'\sin k_2 d'}{Z_2'\cos k_2 d' + iZ_3'\sin k_2 d'}\right) \tag{4.7}$$

where k_2 is the wave number in a medium 2. The transmission is given by,

$$T = \frac{2Z_3''}{Z_3'' + Z_1'} \tag{4.8}$$

For the unpumped and pumped structures which have five and three interfaces respectively, Equation 4.7 has been used sequentially starting at the last optical surface and working back to the first. The respective impedances are given in Equations 4.9 (a) and (b).

$$Z_6'''' = Z_2\left(\frac{Z_6''''\cos k_2 d_2' + i\sin Z_2'\sin k_2 d_2'}{Z_2'\cos k_2 d_2' + i\sin Z_6''''\sin k_2 d_2'}\right) \tag{4.9a}$$

$$Z_4''' = Z_2\left(\frac{Z_4''\cos k_2 d_2' + i\sin Z_2'\sin k_2 d_2'}{Z_2'\cos k_2 d_2' + i\sin Z_4''\sin k_2 d_2'}\right) \tag{4.9b}$$

It should be noted that for the differential transmission (multiline visible Argon pump-THz probe) measurements, it is assumed that the layer underneath the oxide is one continuous layer. This is justified since our probing wavelength is much larger than the thickness of the p+ layer. In addition to this, we assume that the p+ layer is so heavily doped that the electron hole concentration near the surface is far greater than deep into the substrate which allows us not to make any assumptions on the thickness of the layer. We further simplify our analysis by observing the time domain plots (shown in Figure 4.10) and noting that the only change observed in the THz transmission is a reduction in its amplitude due to its photoexcitation rather than a phase change. Hence, it can be said that the change in the index of refraction due to photo-excitation affects only the imaginary part of the refractive index. Thus,

$$\Delta n = i\Delta k = i\frac{\Delta\varepsilon_i}{2n} \tag{4.10}$$

where $\Delta\varepsilon_i$ is the change in the imaginary part of the dielectric constant of the material due to photo-excitation which is obtained from,

$$\Delta\varepsilon_i = \frac{\left(4\pi\Delta N\frac{e}{m_{eff}}\right)\cdot\Delta\tau}{\omega\cdot[1+(\omega\Delta\tau)^2]} \tag{4.11}$$

where ΔN and $\Delta\tau$ are the changes in the carrier concentration and scattering time respectively due to photoexcitation.

Following this method of analysis, we obtained Drude model fits to linear reflection and transmission scans and it is seen that results agree with experimental measurements. To obtain analytical fits to the differential experiments in order to estimate the number of photoexcited defect states, the analysis was done separately for the pumped and unpumped states and then the difference was normalized to the unpumped measurements. This is justified since we were pumping with a CW laser source. This method also allows us to extract the values of the mobility in the interfacial layer from the carrier scattering time.

The value of the frequency independent characteristic optical constants of the materials of the different layers of the wafer that was used in the calculations is shown in Table 4.1.

Table 4.1 Optical Properties of Materials (*N* is the Doping Concentration)

	Silicon (Si)	SiO_2	HfO_2	Si_3N_4	Photoresist
Refractive Index (*n*)	3.42[98]	1.5[28]	2.1[99]	2.1[100]	1.4[101]
Abs. Coeff. (cm^{-1})	$2.06\text{x}10^{-16}\text{x}N$ [102]	~0.00	$4.89\text{x}10^{3}$ [103]	3.891	11
Mass ratio (m_{eff}/m)	0.26 (*e*), 0.38 (*h*)	-	-	-	-

4.5.3 Advanced Modeling with Diffusion and Effective Medium Approximation

4.5.3.1 Diffusive Effects of the Photoexcited Carriers. The continuity equation describes that a change in carrier density with time is due to the difference in the incoming and outgoing flux of carriers taking into account generation and recombination processes. The flow of carriers and recombination and generation rates are shown in Figure 4.6.

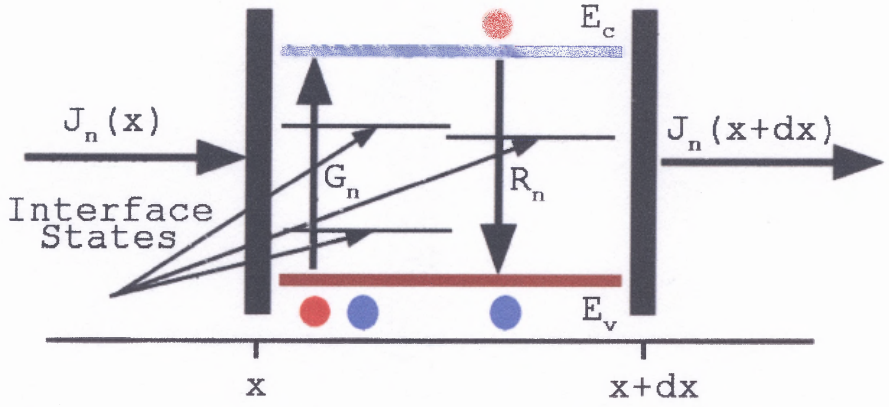

Figure 4.6 Electron currents and possible generation and recombination processes. The interface states have also been shown to demonstrate their position at the gate dielectric/substrate interface.

When the pump laser (CW Argon laser) is incident on the front face of the sample, there is a decrease in the intensity of the beam according to Beer-Lambert's law, $I=I_0e^{-\alpha z}$ where the absorption coefficient of the medium is α and I is the intensity of the radiation at a distance z from the point where the intensity of the radiation is I_0. This concentration gradient of the optical energy due to the optical pump beam accounts for the variation in the number of photoexcited carriers generated at the surface of the interfacial layer than in the bulk of the same layer. The carriers generated at the surface will gradually diffuse into the layer.

In the following analysis, diffusive effects in the HfO_2 layer, the interfacial layer between HfO_2 and p+ Silicon layer and the p+ Silicon layer have been accounted for since the calculations show that the effects of the pump beam will not go beyond 50 nm of the p+ Silicon layer and there is no evidence in literature to show that the pump beam will produce carriers in the photoresist layer.

Once the steady state has been reached, the diffusion equation for the photoexcited carriers takes the form[104],

$$D_n \frac{d^2 n_n(x)}{dx^2} = \frac{n_n(x) - n_n(0)}{\tau_n} \tag{4.12}$$

In the above equation, the subscript n refers to electrons, where D_n is the diffusion coefficient of the electron and τ_n refers to the electron scattering time. A similar equation can be written for the positive carriers or holes. Assuming that we are interested in the region $x>0$ and the fact that the concentration of the carriers has to decrease as we go deep into the medium, the solution to this second order differential equation is,

$$n_n(x) = Ae^{-\frac{x}{L_n}} \tag{4.13}$$

where $L_n = \sqrt{D_n \tau_n}$ is the characteristic diffusion length of the electron in a particular medium and $n_n(x)$ is the concentration of the electrons at a distance x from the surface of the medium. Further, the diffusion coefficient is related to the mobility of the carriers in a particular layer by the Einstein relations[104]. Hence, it is understood that due to the diffusion, there is a non-uniform distribution of the carriers along different points of the same layer, that is, along the direction of propagation of the pump beam through the sample.

This effect of diffusion of the carriers is accounted for in the analysis by incorporating the right hand side of Equation 4.13 in the imaginary part of the dielectric constant of a particular layer given in Equation 4.2. Since we are interested in the number of defects in the interfacial layer between the gate dielectric and the p+ Silicon layer, we assume that there is a change in the diffusion coefficient of the carriers in this particular

layer due to photoexcitation. This is justified as more carriers having energies in the THz range are generated when the laser light is incident on the sample which is also evident from the experimental measurements as shown in Figure 4.10). From the figure, it is observed that when the sample is photoexcited, the amount of THz radiation transmitted is much less compared to similar linear measurements.

However, there is the issue of the dielectric constant of the interface layer which must be calculated to a reasonable degree of accuracy to correctly estimate the actual number of defect states in the interfacial layer between the gate dielectric and the substrate and this forms the subject of the next section.

4.5.3.2 Estimation of Dielectric Constant using Effective Medium Approximation.

The dielectric response of a heterogeneous material and the limits to the amount of microstructural information that can be drawn from it are easily understood if we recall that electrodynamics deals with macroscopic observables that are basically averages of their microscopic counterparts. The solution to the effective dielectric problem therefore, involves two distinct steps: first, the electrostatic problem is solved exactly for the given microstructure to obtain the local electric field ***e(r)*** and dipole moment ***p(r)*** per unit volume at every point in space; secondly, these microscopic solutions are averaged to obtain their macroscopic counterparts[105, 106].

The Lorentz-Lorentz (LL), Maxwell-Garnett (MG) and Bruggeman (BG) effective medium approximation models are simple effective medium theories[107] that represent a heterogeneous dielectric mixture by a single parameter. Hence, they represent a natural first approximation to model the dielectric constant of the interfacial layer between the substrate and the gate dielectric material. The situation is similar to that of a

binary disordered material consisting of two materials having dielectric functions $\varepsilon_1(\nu)$ and $\varepsilon_2(\nu)$ with concentrations (volume fractions) of f_1 and f_2[107, 108, 109].

In the LL approximation, which was developed to describe point polarizable entities of polarizability α embedded in vacuum with $\varepsilon_h=1$, the effective dielectric constant is given by,

$$\frac{\varepsilon_{eff}-1}{\varepsilon_{eff}+2}=f_{HfO_2,SiO_2}\frac{\varepsilon_{HfO_2,SiO_2}-1}{\varepsilon_{HfO_2,SiO_2}+2}+f_{Si}\frac{\varepsilon_{Si}-1}{\varepsilon_{Si}+2} \tag{4.14}$$

The MG approximation assumes that the different materials involved consist of regions large enough to possess their own dielectric identity. If the host dielectric medium (for our case, Silicon) has a dielectric function of ε_{Si} the effective dielectric constant is given by,

$$\frac{\varepsilon_{eff}-\varepsilon_{Si}}{\varepsilon_{eff}+2\varepsilon_{Si}}=f_{HfO_2,SiO_2}\frac{\varepsilon_{HfO_2,SiO_2}-\varepsilon_{Si}}{\varepsilon_{HfO_2,SiO_2}+2\varepsilon_{Si}} \tag{4.15}$$

The BG expression allows the effective medium itself to act as the host medium and in this approximation, the effective dielectric constant of the interfacial layer for the wafers under investigation is given by,

$$f_{HfO_2,SiO_2}\frac{\varepsilon_{HfO_2,SiO_2}-\varepsilon_{eff}}{\varepsilon_{HfO_2,SiO_2}+2\varepsilon_{eff}}+f_{Si}\frac{\varepsilon_{Si}-\varepsilon_{eff}}{\varepsilon_{Si}+2\varepsilon_{eff}}=0 \tag{4.14}$$

where in all the above expressions, HfO_2 and SiO_2 refer to the gate dielectric of the particular wafer under consideration. Equation 4.14 approximates an aggregate or random mixture microstructure where HfO_2 and SiO_2 are inserted into the effective medium itself. Since the interfacial layer in our case is not a guest-host configuration, which is typical to the description of nanomaterials using LL or MG models[110, 111], the BG approximation has been used to model the experimental data.

It should be remembered that the application of the effective medium approximation is justified since the size of the inhomogeneities (~few nm) is well below the wavelength of the probing radiation (~hundreds of microns). Also, as a first order approximation, it has been assumed that the interfacial layer is free of any voids.

The incorporation of diffusion effects and the Bruggeman Effective Medium approximation gives the most accurate results for modeling the results of the differential measurements as has been shown in Section 4.6.

4.5.4 Evaluation of the Number of Interface Traps

Assuming that the recombination time of the carriers in the interfacial layer between HfO_2 or SiO_2 and p+ Silicon layer to be the same, the following expression can be written for the number of interface traps[94, 95],

$$\frac{\sigma(HfO_2)N_{IT}(HfO_2)}{\sigma(SiO_2)N_{IT}(SiO_2)} = \frac{\Delta N(HfO_2)}{\Delta N(SiO_2)} \tag{4.15}$$

where σ is the photon absorption cross-section, N_{IT} is the number of interface traps and ΔN is the number of photoexcited states.

4.6 Experimental Results and Analysis

4.6.1 Linear Time Domain Measurements

As mentioned in Section 4.2, two types of experiments were performed on the samples. This section shows the results of the linear THz transmission experiments.

Figure 4.7 shows the results of the linear time domain scans in reflection mode on the different wafers. As is seen, the experiment was performed in such a manner that the THz beam arrived on all the samples at the same time as without them.

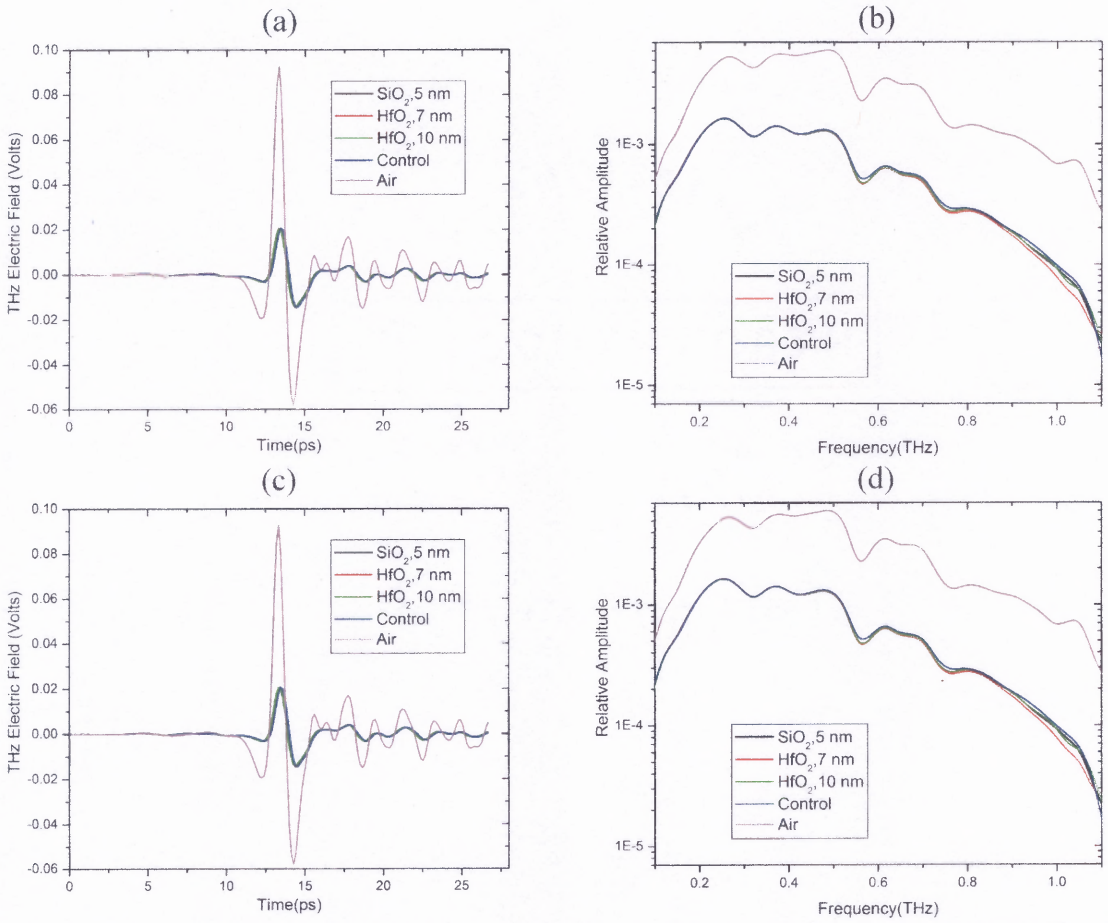

Figure 4.7 Results of reflection measurements on the gate dielectric wafers. (a) the time domain scans, (b) the corresponding Fourier transforms having Si_3N_4 coating as the topmost layer and (c), (d) corresponding measurements for the photoresist coated wafers.

As is observed from the above results, the different types of wafers cannot be distinguished under such measurements. This is also reflected in the reflection spectrum of the same as shown in Figure 4.8. The reflection spectra have been normalized to the spectra of the gold mirror.

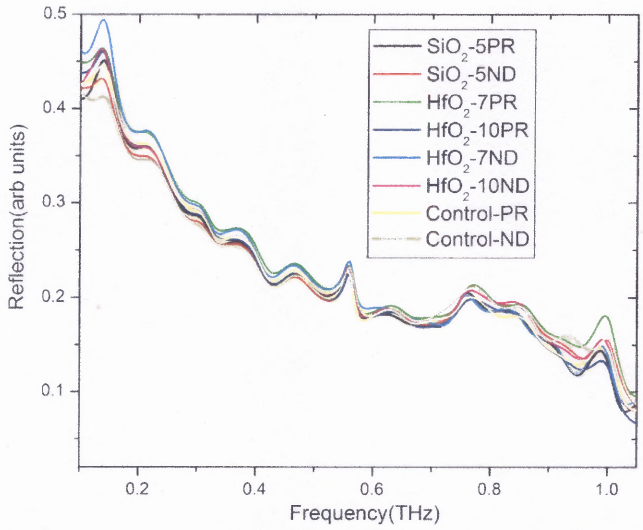

Figure 4.8 Reflection spectrum of the different wafers of the gate dielectrics. The numbers in the legend for each of the wafers refers to the thickness of the gate dielectric layer in nanometers; PR: photoresist coated and ND: Si_3N_4 coated.

Figure 4.9 (a) shows the results of the transmission measurements on the same set of wafers and Figure 4.9 (b) shows the results of the Drude model fit using the impedance matching approach as discussed in Section 4.5.2.2.

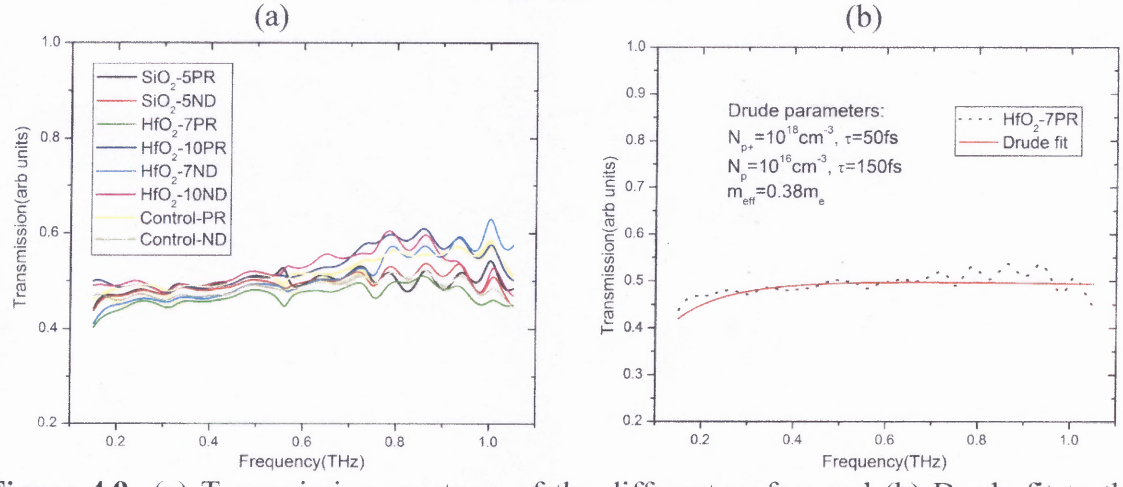

Figure 4.9 (a) Transmission spectrum of the different wafers and (b) Drude fit to the experimental data for wafer with a 7 nm layer of HfO_2 coated with photoresist.

Once again, it is seen that the various wafers appear similar under linear transmission measurements. The Drude parameters obtained from the fit, namely, the carrier concentration N_{p+}, N_p and the respective scattering times τ match closely with the specifications provided by the manufacturer and have been used for subsequent calculations in the analysis of the data obtained from differential measurements.

It is observed from the graphs shown in Figures 4.8 and 4.9 that the scatter is more in the case of transmission measurements which can be attributed to the fact that the spot size of the THz beam is only 3 mm for transmission measurements compared to 45 mm for reflection measurements. This results in the transmission experiments to be more sensitive to film inhomogeneities, surface roughness and other physical attributes.

4.6.2 Optical pump-THz probe measurements

Figure 4.10 shows the time domain plots of optical pump-THz probe measurements on the set of wafers. As mentioned earlier, the optical pump was a multi-line visible CW Argon laser at 514 nm with an intensity of 0.5 W/cm^2.

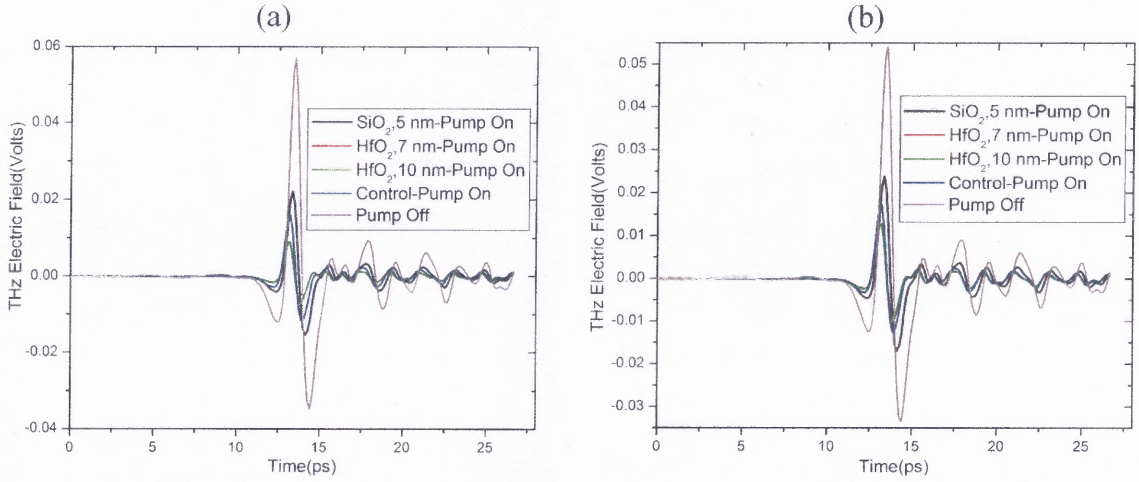

Figure 4.10 Experimental plots of visible pump-THz probe on the gate dielectric wafers for (a) Si_3N_4 coated and (b) photoresist coated wafers.

It can be seen from the graphs that even though, the wafers all looked similar under linear reflection and transmission measurements, there are pronounced differences between them under optical pump-THz probe measurements. Also, the most dominant effect observed is a change in amplitude of the THz waveform which suggests that the change in transmission is mainly due to the imaginary part of the dielectric constant as mentioned in Section 4.5.2.2.

The differential plots as shown in Figure 4.11 have been constructed by taking the difference of the experimental measurements for the case when the pump beam was on to the case when the pump beam was off and then this difference was normalized to the pump beam off situation. This calculation is expressed in the following equation,

$$\text{Normalized Differential Field, } D_{THz} = \frac{E_{\text{pump on}} - E_{\text{pump off}}}{E_{\text{pump off}}} \tag{4.16}$$

It is observed from the plots that the differences between the wafers are more evident under visible pump-THz probe measurements. It is even possible to distinguish between the photoresist coated and the Si_3N_4 coated wafers.

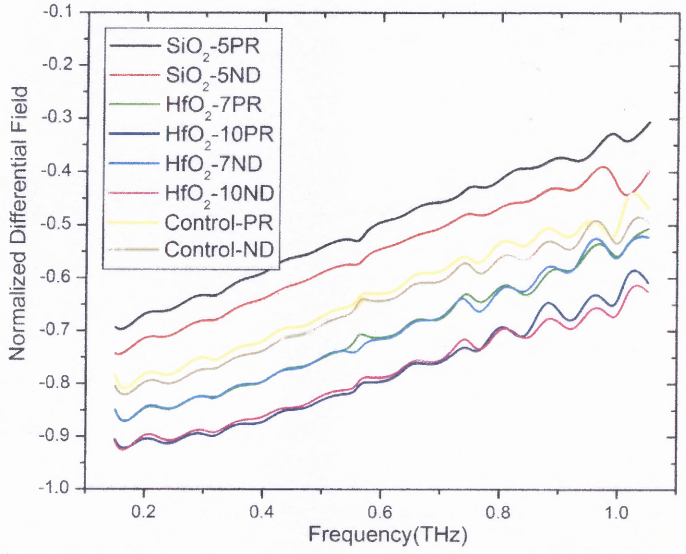

Figure 4.11 Differential plots for the sets of wafers under visible excitation of 0.5 W/cm^2. Clear differences can be observed between the different sets of wafers.

4.6.3 Analysis of Experimental Data

Preliminary modeling using the method of transfer matrices gives results as shown in Table 4.2. The details of the calculations have been shown here[94, 95]. As is seen from the table, the number of photoexcited carriers is too large. Though it is possible that carriers are generated at the rate of 10^{18}/second, diffusive effects will reduce the number of carriers that is seen by the THz probe pulse. At the same time, this model assumed that the scattering time of the carriers in the interfacial layer for both the SiO_2/Si and the HfO_2/Si interface is the same. Since the model did not account for any difference in the scattering time of the carriers (it was assumed to be 200 fs), we were not able to make any estimate of the mobility in the interfacial layer.

Table 4.2 Parameters Extracted by the Transfer Matrix Method

Wafer	No. of photoexcited states(cm^{-3})
Silicon Dioxide(PR)	$3x10^{16}$
Silicon Dioxide(ND)	$8x10^{16}$
Hafnium Dioxide(PR)	$3x10^{17}$
Hafnium Dioxide(ND)	$4.8x10^{17}$
Control(PR)	$1.7x10^{17}$
Control(ND)	$2x10^{17}$

The more general modeling involving the impedance matching approach incorporated the variation of the scattering time for the different layers and it gave better estimates of the number of photoexcited defect states. Additionally in accordance with Equation 4.11, the algorithm automatically calculated the scattering times for the

different interfacial layers (namely HfO_2/Silicon and SiO_2/Silicon) from which an estimate of the mobility of the interfacial layer was also possible by using the equation,

$$\mu_{e,p} = \frac{e\tau_{e,p}}{m_{e,p}}, \tag{4.17}$$

where the subscripts e and p refer to electrons and holes respectively. Theoretical fits to the experimentally obtained data for visible pump-THz probe measurements is shown in Figure 4.12 and the corresponding number of defect states and extracted mobility values have been tabulated in Table 4.3. The number of photoexcited defect states for the HfO_2/Silicon interface is found to be at least ten times more than for the SiO_2/Silicon interface. However, the number is too high considering the fact that our pump beam was continuous. At the same time, the results of the number of defect states are off by at least a few orders of magnitude from the expected theoretical values which are typically of the order of 10^{12} cm^{-3} for the HfO_2 coated wafers[80]. This is expected because Equation 4.15 assumes that the scattering times are similar for all the wafers.

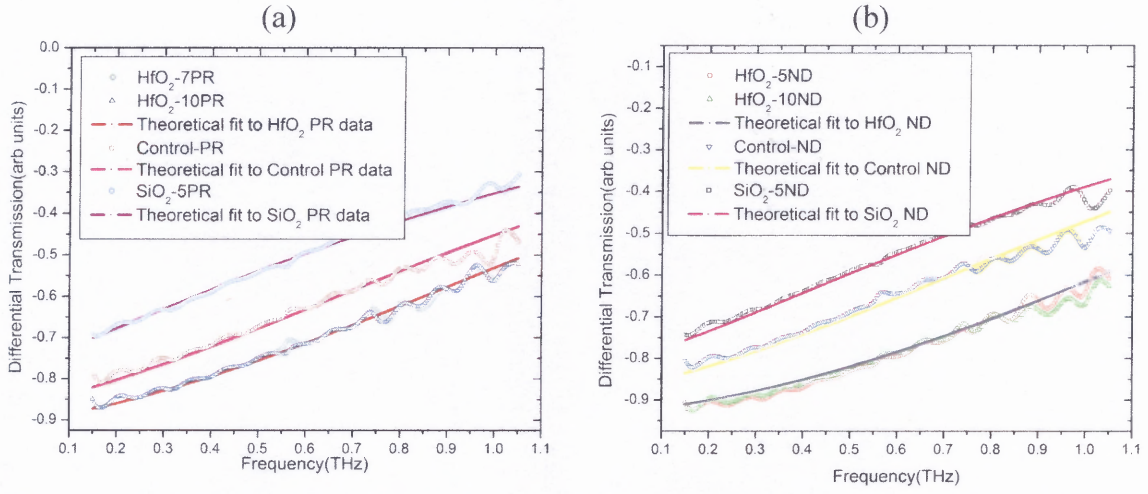

Figure 4.12 Differential plots and theoretical fits for (a) Photoresist coated samples and (b) Si_3N_4 coated samples. It can be seen that using the simple analysis as described in the text in Section 4.5.2.2, accurate fits are generated by changing the carrier concentration and scattering times for the different wafers.

Table 4.3 Defect States and Mobility for Different Wafers(Preliminary Analysis)

Wafer	No. of defect states(cm^{-3})	Mobility(cm^2/V-s)
Silicon Dioxide(PR)	$3.0x10^{14}$	450
Silicon Dioxide(ND)	$8.0x10^{14}$	430
Hafnium Dioxide(PR)	$3.0x10^{15}$	240
Hafnium Dioxide(ND)	$4.8x10^{15}$	210
Control(PR)	$1.7x10^{15}$	225
Control(ND)	$2.0x10^{15}$	210

Finally, on applying the model as developed in Section 4.5.3, it is seen that the incorporation of diffusive effects and the BG effective medium approximation, the most accurate results are obtained because the effect of diffusion allows us to estimate the exact number of photoexcited defect states and since it has been assumed that the interfacial layer behaves as a Bruggeman effective medium with a mixture of Silicon dioxide and Hafnium dioxide it was also possible to estimate the thickness of the interfacial layer with a fair degree of accuracy. Figure 4.13 shows the corresponding graphs for the different sets of wafers. It is evident from the graphs that there is an excellent match of the theoretical model with the experimentally observed differential transmission.

Table 4.4 lists the number of defect states, electron mobilities and the thickness of the interfacial layer for each of the wafers. Interestingly, the results agree with the values obtained by electrical measurements on similar wafers performed at Sematech Inc.[112] and as reported by other researchers working on similar structure wafers[113, 114, 115].

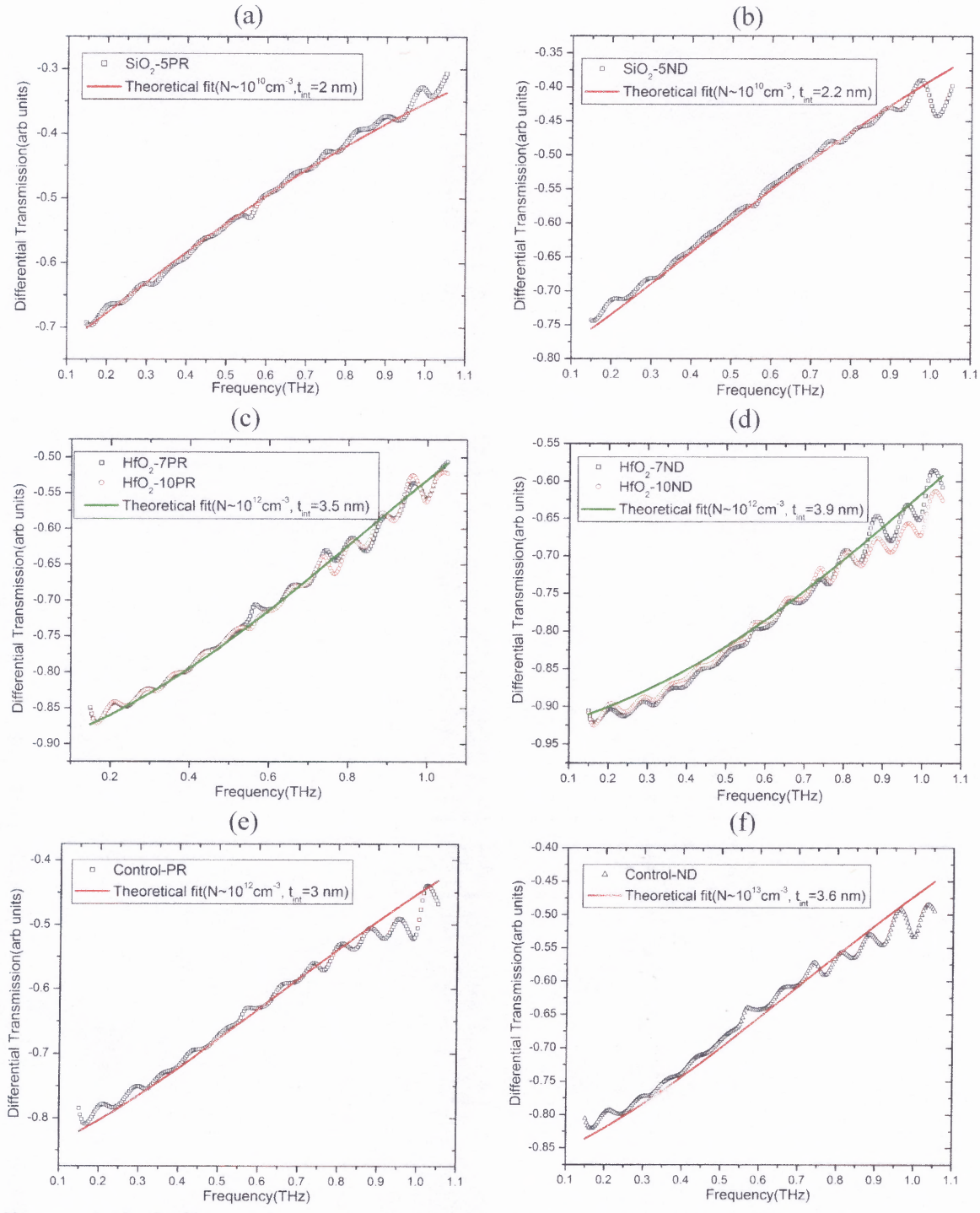

Figure 4.13 Differential experimental measurements and corresponding theoretical plots for (a), (c), (e) photoresist coated wafers (PR) and (b), (d), (f) Si_3N_4 coated wafers (ND). The fitting parameters have been included in the legend for easy reference. It is seen that in all the cases, the thickness of the interfacial layer for ND coated wafers is more than in the case of corresponding PR coated wafers. It would not be out of point to mention that the fits are more sensitive to the thickness of the interfacial layer than to the defect density at the interfacial layer.

Table 4.4 Parameters of the Interface (Advanced Analysis)

Gate Dielectric	No. of Defect States(cm^{-3})	Mobility(cm^2/V-s)	Interfacial layer thickness(nm)
SiO_2(PR)	$2.5x10^{10}$	450	2.0
SiO_2(ND)	$3.0x10^{10}$	430	2.2
HfO_2(PR)	$5.5x10^{12}$	240	3.5
HfO_2(ND)	$8.0x10^{12}$	210	3.9

4.7 Conclusions

Continued scaling of the gate dielectric has precipitated the need for a greater and more detailed understanding of the issues pertaining to integration and reliability. In this work, an all optical non contact technique has been proposed to estimate the number of defect states and the thickness of the interfacial layer for a stacked dielectric structure. The dielectrics studied are the present day industry standard, SiO_2, and the most promising replacement candidate of the future, HfO_2.

It was also observed that photoresist coated samples are more transmissive to THz radiation than the corresponding Si_3N_4 coated samples. This is probably due to the fact that photoresist is more absorptive to visible wavelengths than Si_3N_4. Also, we have been unable to distinguish between the wafers having different thickness of the gate dielectric material, namely, HfO_2. This is expected since we are probing the dynamics of the carriers underneath this layer or of the "buried" layer. Also, not much difference is expected in the number of photoexcited carriers between the 7 and 10 nm thickness of the material.

The results obtained are very promising as they show the immense potential of a myriad of applications THz spectroscopy in the semiconductor industry. This study opens up the possibility of using THz radiation to study the properties of "buried" layers which might be of immense help in the microelectronics industry for in-situ monitoring of the quality of the fabricated wafers and also for semiconductor metrology applications.

CHAPTER 5

CHARACTERIZATION OF MATERIALS OF CONTEMPORARY INTEREST

As mentioned previously in this dissertation, the core objective of this work has been to characterize different materials in terms of their material properties that will help in their classification and subsequent identification.

To that effect, in the first part of the current chapter, we discuss our attempt to observe differences, if any, in the absorption spectrum of a chemical (Ammonium Nitrate, NH_4NO_3) having different grain sizes. The second part deals with our experiments using another chemical (Composition C-4; which is essentially hexahydro-1-3-5-trinitro-1-3-5-triazine or RDX). Finally, the last portion of this chapter discusses about our investigation on a novel material, cyclic olefin polymers, using THz spectroscopic techniques.

5.1 Investigation of Ammonium Nitrate

5.1.1 Introduction and Motivation

Over the past several years, there has also been an increased interest in the potential of using THz radiation in applications such as medical imaging and tomography[116], spectroscopy and detection of concealed explosives, chemical and biological agents and common biomaterials[117, 118, 119]. The major factors contributing to this interest are:

(a) Material Transparency: THz radiation is transmitted through most non-metallic and non-polar mediums, thus enabling THz systems to "see through" concealing barriers such as packaging, corrugated cardboard, walls, clothing, shoes, book bags, pill coatings etc. in order to probe for concealed or falsified materials.

(b) Spectroscopic Signatures: Many materials of interest for various applications (eg. explosives, chemical agents, and biological agents for security applications, and pharmaceutical chemicals for online monitoring/ control) have characteristic THz spectra that can be used to fingerprint and thereby identify these materials.

In the study of solids, THz spectroscopy is particularly relevant as the observed absorption features could be linked to the states of crystallinity and morphological conditions of the solid under study[120, 121]. Most of the solids under THz studies have grain sizes that are comparable to the wavelength of THz waves and thus, size dependant characteristics like the complex refractive index play a major role in determining the material transmission and extinction spectra. In such cases, the extinction spectra are greatly influenced by scattering losses which partially obscure the characteristic phonon resonances of the solids leading to complications in the quantitative analysis of the experimental data[122].

Driven by the motivation of resolving the above limitations, we carried out THz spectroscopic measurements with NH_4NO_3; the identification of which is further complicated by its lack of having any sharp spectral signatures at THz frequencies. Fourier Transform Infrared (FTIR) studies have already reported that NH_4NO_3 has monotonically increasing attenuation spectra up to 3 THz[117]. The usefulness of experimental measurements where the grain size of the solid is varied to identify any trend in the transmission and/or extinction spectrum thus bears particular interest in the THz region as it would set the fundamental limitations on the absorption signature of these materials.

In this study, the transmission spectrum of Ammonium Nitrate has been obtained for different grain sizes to study the effects of scattering between 0.2 and 1.2 THz. It is

also shown that when the grain size of the sample is increased, there is a deviation from the Mie theory prediction.

5.1.2 Experimental Methodology

The experimental set-up is similar to the arrangement that has been described earlier in Section 3.1.2 and will not be repeated here. The sample of NH_4NO_3 was obtained from Fisher Scientific® (CAS # 6484-52-2) and was of average grain size 700-750 μm. This was spread out uniformly in three sets of samples over Scotch® polyethylene packaging tape. The first set of the samples had a thickness of 1.602 mm. The next two sets were crushed using mortar and pestle to an average grain size of 350-400μm, thickness: 0.380 mm and 100-150μm, thickness: 0.413 mm respectively. Scotch® packaging tape was used as the sample holder and the two tapes sticking together was used as the reference or "blank" for the measurements.

The standard procedure of making pellets mixed with high density polyethylene (HDPE) using a pellet press was avoided in order to maintain control over the grain sizes. Moreover, it has been reported that inexact mixing of PE powder and the compounds affects the absorption spectra[123].

5.1.3 Experimental Results and Analysis

As noted earlier, time resolved THz spectroscopy provides both amplitude and phase information about the samples under study. Figure 5.1 (a) shows the THz electric field amplitude of the three different samples of NH_4NO_3 and the "blank". The delay in the arrival time of the THz pulse gives an estimate of the broadband refractive index of NH_4NO_3 to be 1.804 which compares well with the literature value of 1.816[124]. The

corresponding amplitude spectrum obtained by Fourier transforming the time domain data is shown in Figure 5.1 (b).

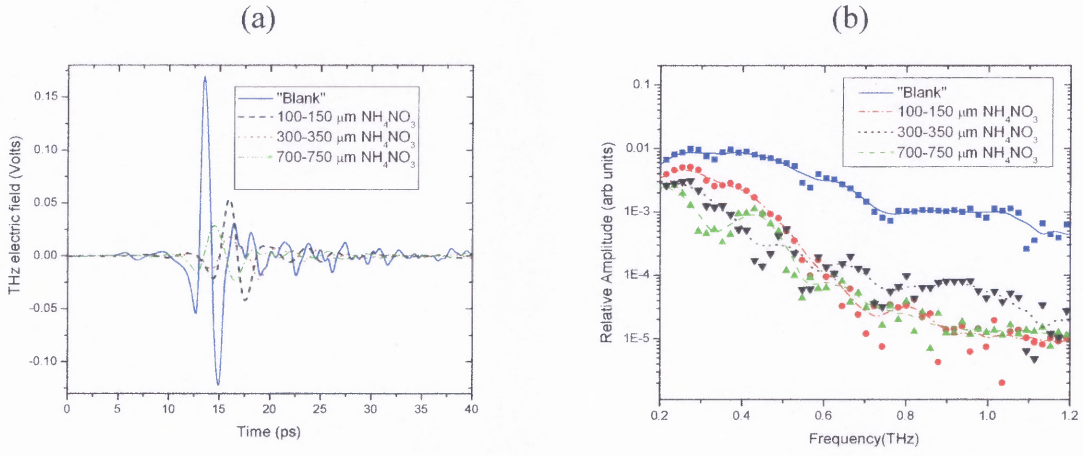

Figure 5.1 Plots of the THz signal in (a) time domain and (b) frequency domain. The dips of the reference pulse at 0.57 THz, 0.78 THz and 1.12 THz are due to water vapor absorption.

The transmission spectrum $T(\nu)$ for each of the samples of NH_4NO_3 is obtained from the following equation,

$$T(\nu) = \frac{\left|E_{sample}(\nu)\right|}{\left|E_{reference}(\nu)\right|} \tag{5.1}$$

Figure 5.2 shows the transmission spectrum of NH_4NO_3 for the three different grain sizes. A significant trend is observed where it is found that the width of the transmission spectra decrease with increase in size of the grains. Subsequent numerical fits also shown in Figure 5.2 reveal that the frequency dependence of the transmission spectrum is such that, when the grain size is small (100-150μm), it follows the inverse square law which is not in accordance with Rayleigh scattering[122, 125]. However, with an increase in grain size, the dependence tends to be of an inverse cubic nature.

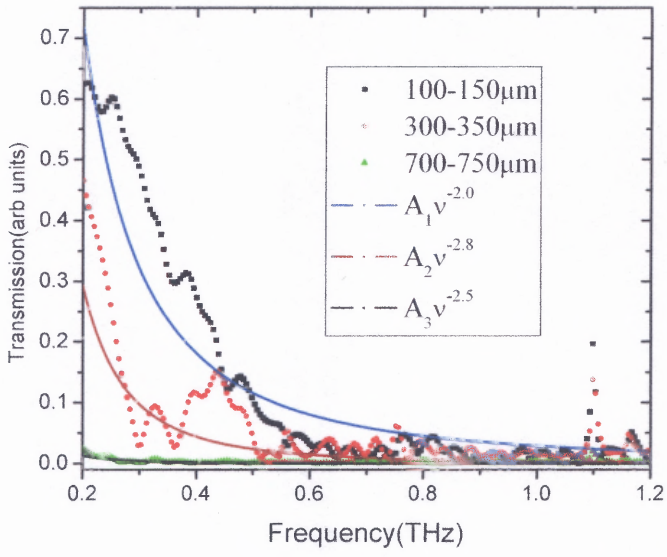

Figure 5.2 Plot of the THz transmission spectra of NH_4NO_3. The scatter show the experimental points for the different grain sizes and the corresponding lines show the numerical fits in accordance with the legend of the figure.

From the numerical fits, it can be seen that when the grain size of NH_4NO_3 is small (100-150μm), the results cannot be modeled on the basis of Rayleigh theory which says that the optical scattering of a collection of scatterers depends inversely on the fourth power of the frequency. Hence, the Mie theory was applied since it accounts for the variation in the frequency dependence of the optical transmission based on both the grain size and refractive index of the materials[126]. Figure 5.3 (a) shows the extinction spectrum for NH_4NO_3 for different grain sizes and Figure 5.3 (b) shows the corresponding predictions based on Mie theory for the 100-150 μm grain size sample. A detailed analysis based on the Mie theory approach can be found here[127].

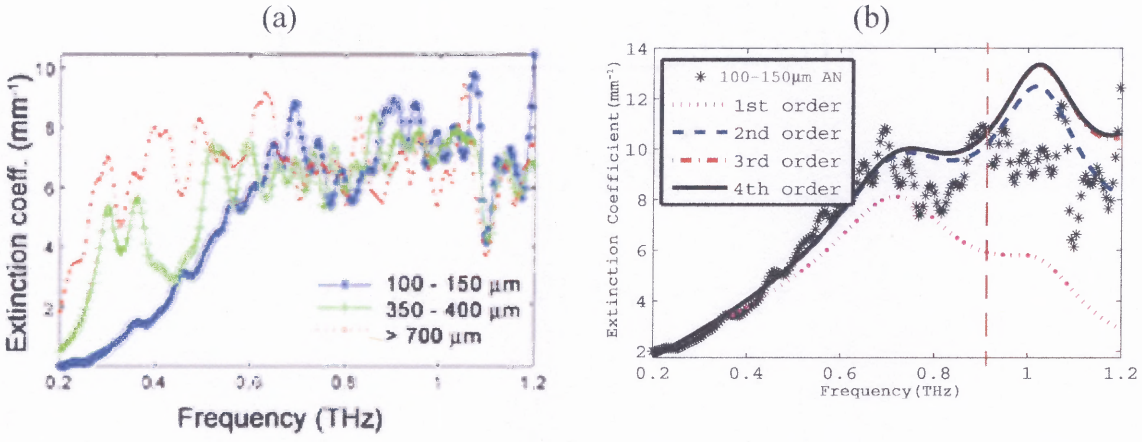

Figure 5.3 (a) Experimental extinction for the different grain size samples of NH_4NO_3 and (b) Experimental and theoretical predictions of extinction coefficients for 100-150 μm grain size of NH_4NO_3. The red line in (b) shows the region of validity of Mie theory. The stars show the experimental points and the lines show different orders of fit to the Mie theory model.

Subsequent work at the THz Spectroscopy and Imaging Group at NJIT plotted a generic curve based on Mie theory[127]. This plot predicts the total extinction coefficient for different materials, M with refractive indices n, and a range of values of size parameter, x, to account for any variation of their size and/or wavelength as shown in Figure 5.4. In this plot $x = 2\pi\nu r / c$ is the size parameter which is defined as the ratio between the size of the grain and the center wavelength of the probing radiation, is an important dimensionless quantity.

This work showed that these frequency trends are not unique or representative of the materials used, as extinction is a function of the refractive indices, n and as well as the size parameters, x of the samples. In fact, for a specific material with different grain sizes, one would obtain varying frequency dependence of extinction. Likewise, the grain sizes of different materials could be chosen in such a way that the extinction spectra of all those different materials with varying grain sizes would show a particular frequency trend.

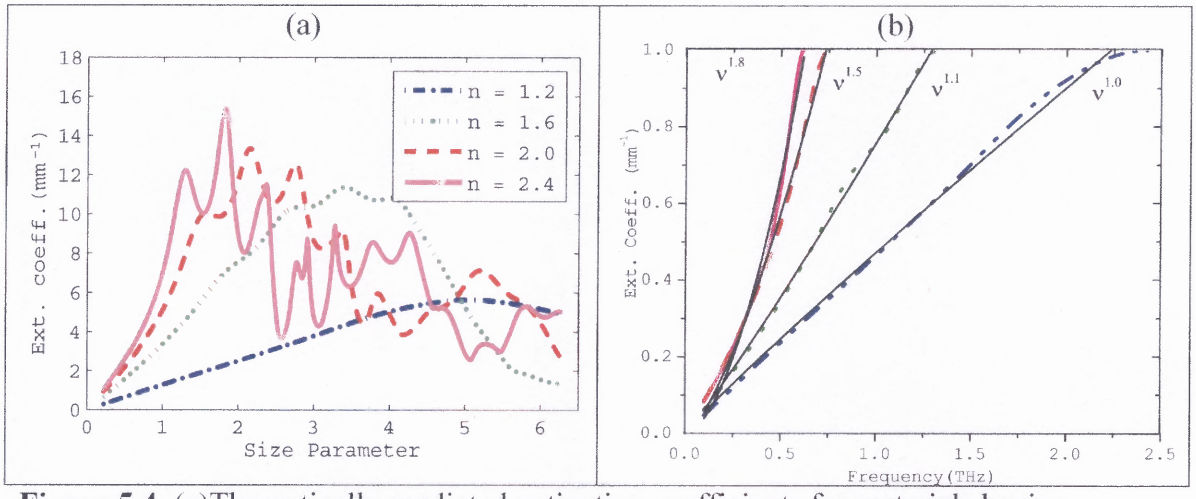

Figure 5.4 (a)Theoretically predicted extinction coefficients for materials having refractive indices, *n* and size parameters, *x*; and (b) the normalized extinction coefficient for a grain size of 100μm as a function of frequency.

5.1.4 Conclusions

In this study, the transmission spectrum of Ammonium Nitrate has been obtained for different grain sizes to study the effects of scattering between 0.2 and 1.2 THz. It is shown that with increasing grain size, there is a deviation from the Mie theory prediction which can be attributed to the fact that larger grains have arbitrary shapes which are not essentially spherical and thus, Mie theory does not appear to hold for them. In a more physical sense, it can be argued that larger grains introduce the effects of dependent scattering, multiple scattering and other factors making the radiation transfer problem more complex.

Finally, it can be deduced from this study that any identification of an unknown granular solid in a concealed manner cannot be made based on the frequency trend of its THz extinction spectra, as the frequency dependence of the extinction of a solid is a function of both its material property, as well as its grain size. This work, might therefore, prove to be a crucial step towards successful material identification with its

attempt to enumerate the possible discrepancies in the spectrum due to different morphological conditions.

5.2 Investigation of hexahydro-1-3-5-trinitro-1-3-5-triazine (RDX)

5.2.1 Introduction and Motivation

THz pulsed spectroscopy and imaging have been identified as very promising techniques for the identification of explosives and other threats in security screening at airports and elsewhere. One of the main advantages of using THz radiation for such applications is THz waves have very low photon energies (4 meV at 1 THz; 1 million times weaker than X-ray photons) and will not cause harmful photoionization in biological tissues[128, 129].

Of particular note are THz applications where the unique interrogation and characterization capabilities of the submillimeter wave radiation has been applied to highly ordered materials, for example, crystalline explosives and drugs that exhibit strong THz absorption features[118, 130, 131, 132] by experimental studies in transmission mode. However, for real-world applications, reflection measurements are preferred since most bulky targets are impossible to measure in transmission mode as the target will attenuate the incident THz waves completely.

In this study, the main motivation was to perform reflection measurements using hexahydro-1-3-5-trinitro-1-3-5-triazine (RDX) and to investigate whether there is sufficient contrast in the measurements around 0.8 THz, the most prominent absorption peak in the THz spectrum of RDX.

5.2.2 Experimental Methodology

The basic principle of the experimental scheme is very similar to the one that is employed in transmission studies as described in Section 3.1.2. However, the modifications that were done to perform reflection measurements are shown in Figure 5.5.

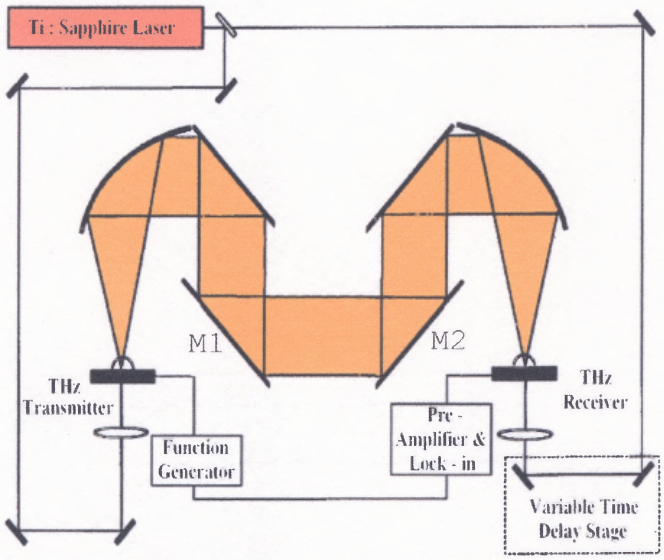

Figure 5.5 Schematic of a THz-TDS system in reflection geometry. All the mirrors used are either gold coated plane mirrors or off axis parabolic mirrors. Mirror M2, a gold coated plane mirror of diameter 2" is replaced by RDX and thus is the reference for the measurements.

The sample of RDX used was a circular disc of diameter 1 inch and thickness of 1 mm. it was prepared from a spherical mass of Composition C-4 (91% RDX and 9% plasticizer) which was eventually flattened over a Teflon plate using a Teflon spatula. Care was taken to make the reflecting surface as uniformly flat as possible.

5.2.3 Experimental Results and Analysis

In THz reflection spectroscopy measurements, one reference waveform, $E_{ref}(t)$ is measured which reflects from the surface of the gold mirror and a second measurement, $E_{sample}(t)$ is performed, in which the THz radiation reflects off the sample. The reflection spectrum $\tilde{R}_{\exp}(\nu)$ is obtained from the FFT of the time domain data as,

$$\tilde{R}_{\exp}(\nu) = \left(\frac{|E_{sample}(\nu)|}{|E_{ref}(\nu)|} \right)^2 \tag{5.2}$$

To account for the variation of the reflection cross section between the reference and the sample, we introduced a normalization factor, which we considered to be a positive multiplicative constant to the experimental reflectance defined as,

$$R^{+}(\nu) = \tilde{R}_{\exp}(\nu) * (CONSTANT) \tag{5.3}$$

Figure 5.6 (a) shows the THz electric field amplitude of the gold mirror and RDX. The corresponding amplitude spectrum is shown in Figure 5.6 (b).

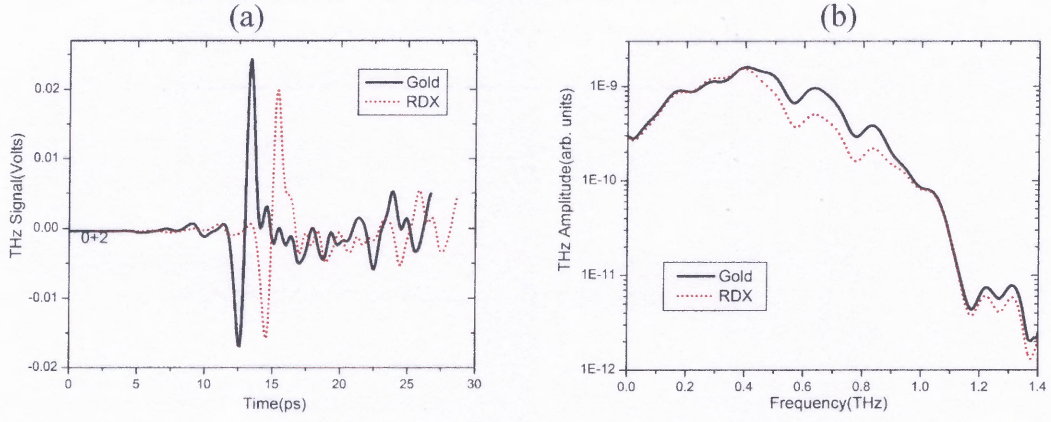

Figure 5.6 THz electric fields for Gold and Composition C-4 and (b) amplitudes of the same. The time domain plots in (a) have been horizontally offset for clarity.

The natural logarithm of the experimentally obtained reflectance as defined in Equation 6.4 has been shown in Figure 5.7.

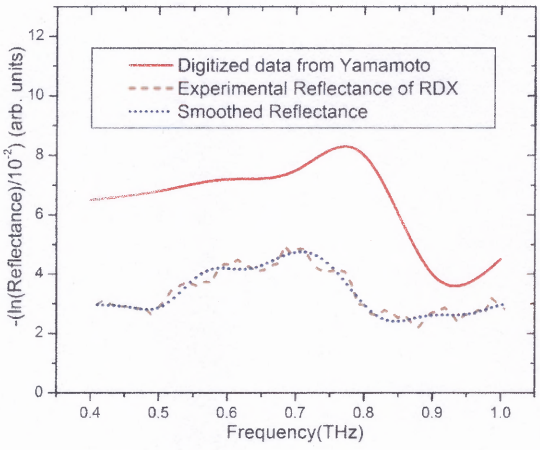

Figure 5.7 Comparison of the experimentally obtained and theoretically predicted reflectance of RDX. The curves have been displaced vertically for clarity.

5.2.4 Conclusions

The results show that a contrast of 8% is observed around the primary absorption peak of RDX, that is, at 0.8 THz and there is an excellent repeatability of measurements. Previous experimental measurements in the THz region involving RDX in both specular[133] and diffuse[134] reflection modes had reported similar results. They agree with the theoretical prediction of Yamamoto where he had used the transmission data and had then, theoretically calculated the expected reflectance of the material. The investigation has demonstrated that THz techniques are promising for the detection of RDX based explosives in the reflection configuration which is significant for stand-off detection and identification in real world applications. However, spectroscopic detection of RDX in reflection requires a system to measure a change in reflection from 0.7-0.9 THz of about 8%.

5.3 Investigation of Cyclic Olefin Polymers

5.3.1 Introduction and Motivation

Optical plastics[135] are an important article of commerce and are widely used to make optical storage devices such as compact discs (CDs) and digital video discs (DVDs)[136], lenses for cameras and projection displays[137], fibers[138] and diffractive optical lenses[139]. The advantages of optical plastics over other materials are their mechanical toughness and high optical transmission[136].

More recently, polymers have found increasing use in optical components and devices such as waveguide integrated optics[140, 141]. The materials for such applications must satisfy many requirements of which the foremost are high use temperature, high optical transmission in the region of interest, low moisture absorption, low birefringence and, in certain applications, a large thermo-optic coefficient[142, 143].

TOPAS® Cyclic olefin polymers (COPs)[144] are a new class of optical thermoplastics that have a number of attractive properties, namely low moisture uptake, high water barrier, low birefringence, high optical transmission, large Abbe number, chemical resistance to common solvents such as acetone and high heat resistance (glass transition temperature T_g=180°C)[145]. TOPAS® has been evaluated highly in the market as a resin with optical properties comparable with PMMA (Polymethyl methacrylate, acrylic resin), superior heat resistance to PC (polycarbonate) and superior dimensional stability to PMMA and PC[135]. Furthermore, it is a material that is suitable for modifier applications for existing materials, where it can improve the water vapor barrier, increase rigidity, enhance heat resistance and make materials easier to cut.

In addition to all the above material aspects of COP, it holds a greater promise in the world of optical characterization where it maybe used for manufacturing broadband window, lens, and optical chambers. This is particularly crucial as COP has a high constant transmission of ~ 90% over the entire range of the visible spectrum as also very low attenuation around the CO_2 laser wavelengths[140, 141].

The main motivation of the current study was to investigate such polymers for their potential use in the THz range of frequencies as that would give tremendous flexibility in terms of it use for spectroscopy and imaging.

5.3.2 Fabrication of Cyclic Olefin Polymers

The sample of TOPAS® COP 8007 was obtained from the Infrared Fibers Group at Rutgers University, New Brunswick. A brief summary of the typical procedure for fabrication of such materials is outlined below.

COP is copolymerized from norbornene and ethylene using a metallocene catalyst in contrast to the more conventional methods used to make other optical plastics[146]. A typical polymerization scheme is shown in Figure 5.8. The presence of norbornene in ethylene does two things: it raises T_g and reduces crystallinity so that when norbornene is present, the polymer is amorphous.

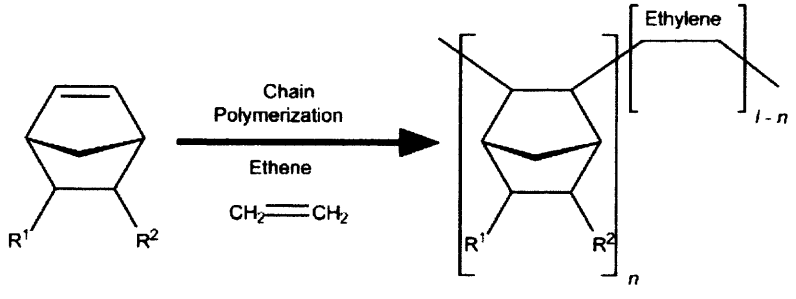

Figure 5.8 Polymerization scheme for manufacture of COP.

5.3.3 Experimental Methodology

The experimental set-up is similar to the arrangement that has been described earlier in Section 3.1.2 and will not be repeated here. By rotating the COP sample at various angles to the incoming THz radiation, variations, if any, on the transmission spectrum has been studied.

5.3.4 Experimental Results and Analysis

Figures 5.9 (a) and (b) show the THz electric field amplitude both with and without the 40 μm thick COP sample placed at the focus of the THz beam and the corresponding transmission spectra for the three different angles. The experiment was also performed with a 3 mm thick bulk COP sample to obtain an estimate of the broadband refractive index of the material from the delay in the arrival time of the THz pulse and it was found to be 1.492 which matches closely with the value at 1 THz as predicted by a Sellmier equation of the form[146],

$$n^2 = A_1 + \frac{A_2 \lambda^2}{\lambda^2 - A_3^2} \tag{5.4}$$

Here, A_1, A_2 and A_3 are the fitting parameters; n is the refractive index and λ is the wavelength in microns. Incidentally, the predicted value is 1.520 with fitting parameters A_1= 2.043, A_2=0.2733 and A_3=0.202[146].

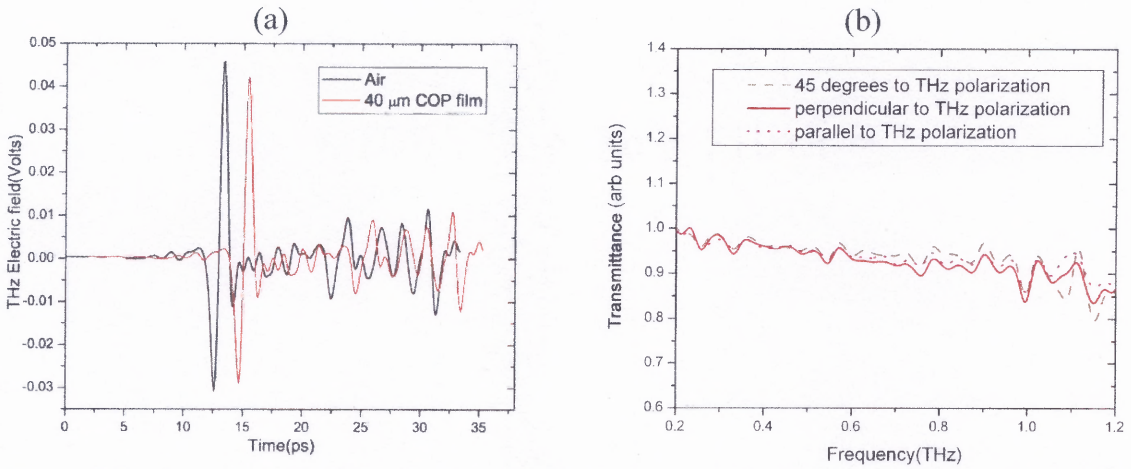

Figure 5.9 Plots of (a) THz Electric fields and (b) transmission spectra of the COP sample at different angles to the incident THz polarization.

It can be seen from the transmission spectra that almost all the incident light (~95%) is transmitted through the polymer and the transmission is also independent of the polarization of the incident THz beam and thus, opens up the possibility of using this material for fabricating THz optics.

In order to extract the frequency dependent optical parameters of TOPAS® 8007 COP film, the analytical recipe as outlined in Section 3.4 of Chapter 3 has been used. The material was optically thin and so it was necessary to account for the Fabry-Perot effects in the refractive index and the extinction coefficient of the material. Figure 5.10 shows the plots of the refractive index and the extinction coefficient of the 40 μm thick cyclic olefin polymer film. It is seen that the typical refractive index is ~ 1.52 which might allow the material to be used for index matching applications and the fact that the extinction coefficient is low (~0.1) hints that it can also be used as a window material in the THz range of frequencies as a cheap alternative to high resistivity float zone Silicon or high density polyethylene (HDPE).

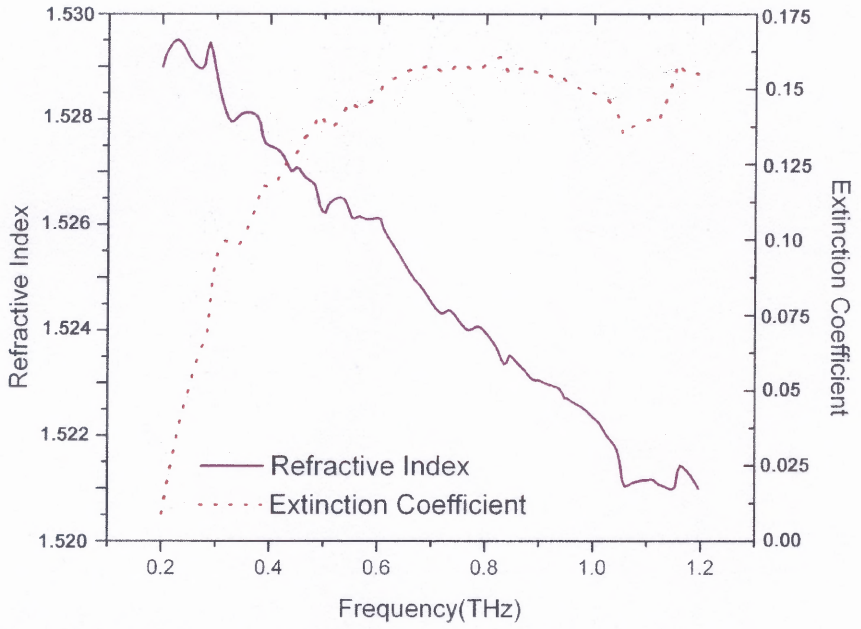

Figure 5.10 Graph showing the variation of refractive index and extinction coefficient of TOPAS® COP film between 0.2 and 1.2 THz.

5.3.5 Conclusions

The current study extends the range of COP transmission to include the far infrared or the THz region of wavelengths where it has been shown that almost 95% of the incident THz radiation passes through the material with very little attenuation. This opens up the unique possibility of commissioning this polymer for transparent optics to be used in such optical systems which would require the use of both high energy radiation such as near-UV and low energy radiation such as THz.

From a more specific point of view in terms of spectroscopic standpoint, COP optics, especially in electro-optic sampling measurements and THz pump-probe investigations would reduce the typical problems of stringent alignment while using different wavelengths of pump radiation through conventional THz optics materials like Silicon or HDPE which are opaque to such wavelengths of radiation.

CHAPTER 6

CONCLUSIONS AND FUTURE PERSPECTIVES

The THz band, bordered by far infrared and millimeter wave bands of the electromagnetic spectrum encompass radiation that fall within an approximate range of 0.3-10 THz, which corresponds to wavelengths between 30 μm and 1 mm. THz spectroscopic technology has advanced to the point where practical commercial systems are now feasible. With this advancement has come the potential for THz imaging, both in the focal plane and using interferometric techniques. Combined they offer a powerful tool for material characterization, inspection and security screening.

This dissertation has proposed systems and algorithms for material characterization and has presented a framework for material identification based on THz spectroscopic data. This framework has been applied in some specific case studies like obtaining the optical constants of Silicon, studying size dependent effects on the THz transmission using Ammonium Nitrate, obtaining the reflectivity of RDX around its phonon resonance of 0.8 THz for imaging applications in security screening and investigating the properties of TOPAS® 8007, an olefin polymer, for its potential applications in fabricating optical materials at THz frequencies. Additionally, the dissertation has also addressed the issue of investigating the properties of "buried" layers using optical pump-THz probe measurements using multilayer wafer structures.

This chapter concludes this dissertation by drawing together the research described in previous chapters and discussing future directions for continued development. Following is the summary of the previous where THz spectroscopy has

been used as a versatile tool for studying some of the fundamental properties of different materials.

- Chapter 3 presents the study of Silicon where a mathematical routine has been proposed to account for Fabry-Perot effects. This gives significantly better results than those which exist in the literature. Also, this study demonstrates that THz spectroscopy is sensitive to surface roughness of the wafers.

- In Chapter 4, the results of the investigation of multilayer wafer structures have been reported. It shows that THz spectroscopic techniques can be used to study the properties of buried layers. The analysis described involves the use of the diffusion equation and the effective medium approximation to predict the defect density and the thickness of an interfacial layer.

- Chapter 5 discusses three different topics: In the first part, it describes the study of Ammonium Nitrate of different grain sizes to look for any possibilities of identification of such materials having no phonon resonances in the THz region. The second part deals with the identification of RDX, an energetic material. It details THz-TDS in reflection mode and the experimental data have been subsequently used in the THz Spectroscopy and Imaging Group at NJIT to perform simulations relating to interferometric imaging. Lastly, this chapter discusses the investigation of the optical properties of TOPAS® 8007 and highlights its applications for fabricating lenses and windows in the THz region of wavelengths.

In all the above studies, sufficient accuracy was demonstrated and they seek to highlight the potential of THz spectroscopic techniques in a myriad of applications pertaining to characterization of materials.

With rapidly developing technology, there are a vest number of open questions and a vast array of potential research problems. This section surveys the scope of the future work in this area and highlights promising extensions of the work presented in this dissertation.

Much of the progress in THz spectroscopy systems in the past decade is attributable to progress in THz sources and detectors, and these remain core areas of development. Both THz spectroscopy and imaging systems will benefit greatly from

future high power THz sources such as quantum cascade lasers and others described in Chapter 2. Higher power sources coupled with more sensitive detectors will result in higher SNR which will increase the sensitivity of measurements. In particular, THz spectroscopy systems will continue to increase in bandwidth and resolution, while reducing in size.

As greater understanding of the interaction of THz radiation with different materials is obtained, it will become increasingly easier to construct a THz spectroscopic database for screening purposes. Also, as this dissertation has demonstrated, the THz technique has proven to be useful for investigation of the properties of both "surface" layers and "buried" or "hidden" layers. This technique therefore, might be of immense help to the microelectronics industry especially in the context that has been discussed in this dissertation where the defect state density was calculated using optical pump-THz probe techniques.

Also, future controlled studies are required to develop an analytical model to estimate the magnitude of surface roughness and to set the limits of the use of THz radiation for such applications. In particular, THz radiation can also be used to probe the breakdown zone in materials by initiating the breakdown with an externally applied electric field and probing the material with THz radiation to gain fundamental insights into the carrier dynamics of the material near breakdown.

The investigation of Ammonium Nitrate of different sizes demonstrated that Rayleigh scattering is not responsible for the attenuation of THz radiation when it propagates through powdered substances. Subsequent work showed that Mie theory is probably more adept to explain the results especially in the limit of the scatterers being

spherical and in the domain of single scattering. However, any classification of materials based on their size and refractive index is a very difficult problem and would require the incorporation of multiple scattering events.

In closing, it would not be out of place to mention that with every technological advance in each region of the electromagnetic spectrum, there have been vast applications of them in scientific and technological advancement. THz science is still in its infancy and continues to grow with every passing moment.

REFERENCES

1. Mittleman D. (ed.), "Sensing with terahertz radiation," Springer, Berlin (2003).

2. Smith P., Auston D. and Nuss M., "Subpicosecond photoconducting dipole antennas," IEEE J. Quant. Electron., **24**, 255-261 (1988).

3. Baker C., Gregory I. S., Evans M. J., Tribe W. R., Linfield E. H. and Missous M., "All optoelctronic terahertz system using low temperature grown InGaAs photomixers," Opt. Exp., **13**, 9639-9644 (2005).

4. Harde H. et al., "THz time domain spectroscopy on Ammonia," J. Phys. Chem. A, 105, 6038-6047 (2001).

5. Bolivar P. H., Brucheseifer M., Rivas J. G., Gonzalo R., Ederra I., Reynolds A. L., Holker M. and Maagt P., "Measurement of the dielectric constant and loss tangent of high dielectric constant materials at terahertz frequencies," IEEE Trans. Microwave Theory Tech., **51**, 1062-1066 (2003).

6. Quema A. et al., "Identification of potential estrogenic environmental pollutants by terahertz transmission spectroscopy," Jpn. J. Appl. Phys. **42**, L932-L934 (2003).

7. Beard M. C. et al., "Subpicosecond carrier dynamics in low temperature grown GaAs as measured by time resolved terahertz spectroscopy," J. Appl. Phys., **90**, 5915-5923 (2001).

8. Watanabe Y. et al., "Component analysis of chemical mixtures using terahertz spectroscopic imaging," Opt. Commun., **234**, 12-129 (2004).

9. Kojima S., Tsumura N., Takeda M. W. and Nishizawa S., "Far infrared phonon-polariton dispersion probed by terahertz time domain spectroscopy" Phys. Rev. B, **67**, 035102-035110 (2003).

10. Jeon T., Kim K., Kang C., Maeng I. H., Son J., An K. H., Lee J. Y. and Lee Y. H., "Optical and electrical properties of preferentially anisotropic single walled carbon nanotubes films in terahertz region," J. Appl. Phys., **95**, 5736-5740 (2004).

11. Robertson W. M., Arjavalingam G., Maede R. D., Brommer K. D., Rappe A. M. and Joannopoulos Y., "Measurement of photonic band structure in a two-dimensional periodic dielectric array ," Phys. Rev. Lett., **68**, 2023-2025 (1992).

12. Aoki T., Takeda M. W., Haus J. W., Yuan Z., Tani M. and Sakai K., "Terahertz time- domain study of pseudo-simple-cubic photonic lattice ," Phys. Rev. B, **64**, 045106-045112 (2001).

13. Nuss M. C., Goossen K. W., Gordon J. P., Mankiewich P. M. and O'Malley M. L., "Terahertz time-domain measurement of the conductivity and superconducting band gap in niobium," J. Appl. Phys., **70**, 2238-2245 (1991).

14. Kaindl R. A., Carnahan M. A., Orenstein J., Chemla D. S., Christen H. M., Zhai H. Y., Paranthaman M. and Lowndes D. H., "Far infrared optical conductivity gap in superconducting MgB_2 films," Phys. Rev. Lett., **88**, 027003-027110 (2002).

15. Kawase K., Ogawa Y., Watanabe Y. and Inoue H., "Non destructive terahertz imaging of illicit drugs using spectral fingerprints," Opt. Express, **11**, 2549-2555 (2003).

16. Chen Y. C., Upadhya P. C., Linfield E. H. and Davies A. G., "Temperature dependent low frequency vibrational spectra of purine and adenine," Appl. Phys. Lett., **82**, 2350-2353 (2003).

17. Huang F., Schulkin B., Altan H., Federici J. F., Gary D., Barat R., Zimdars D., Chen M. and Tanner D. B., "Terahertz study of 1-3-5 trinitro-s-triazine by time domain and fourier transform infrared spectroscopy," Appl. Phys. Lett., **85**, 5535-5538 (2004).

18. Griffiths P. R. and Haseth J. "Fourier transform infrared spectroscopy," Wiley, New York, NY (1986).

19. Auston D. H., Cheung K. P., Valdmanis J. A., and Kleinman D. A., "Cherenkov radiation from femtosecond optical pulses in electro-optic media," Phys. Rev. Lett., **53**, 1555-1588 (1984).

20. Fattinger C. and Grischkowski D., "Point source terahertz optics," Appl. Phys. Lett., **53**, 1480-1482 (1988).

21. Han P. Y., Tani M., Usami M., Kono S., Kersting R., and Zhang X. -C., "A direct comparison between terahertz time domain spectroscopy and fourier transform infrared spectroscopy," J. Appl. Phys., **89**, 2357-2359 (2001).

22. Gruner G. (ed.), "Millimeter and Submillimeter Wave spectroscopy of Solids," and references therein, Springer, Berlin (2002).

23. Brown E. R., Woolard D. L., Samuels A. C., Globus T., and Gelmont B., "Remote detection of bioparticles in the THz region," IEEE MTT-S International Microwave Symposium Digest, **3**, 1591-1594 (2002).

24. Grischowski D., Keiding S., VanExter M. and Fattinger Ch., "Far infrared time domain spectroscopy with terahertz beams of dielectrics and semiconductors," J. Opt. Soc. Am. B, **7**, 2006-2015 (1990).

25. Altan H., Huang F., Federici J. F., Lan A., Grebel H., "Optical and Electronic characteristics of single walled carbon nanotubes and silicon nanoclusters by THz Spectroscopy," J. Appl. Phys., **96**, 6685-6690 (2004).

26. Hermann M., Tani M., Watanabe M., and Sakai K., "Terahertz imaging of powders," IEE Proceedings-Optoelectronics, **149**, 116-120 (2002).

27. Auston D. H., Cheung K. P., and Smith P. R., "Picosecond photoconducting Hertzian dipoles," Appl. Phys. Lett., **45**, 284-286 (1984).

28. Shan J., Nahata A., and Heinz T. F., "Terahertz Time-Domain Spectroscopy based on Nonlinear Optics," J. Nonlinear Opt. Phys. Mater., **11**, 31-48 (2002).

29. Harshimshony D., Zigler A., and Papadopoulos K., "Conversion of electrostatic to electromagnetic waves by superluminous ionization fronts," Phys. Rev. Lett., **86**, 2806-2809 (2001).

30. Ketchen M. B., Grischkowski D., Chen T. C., Chi C. C., Duling I. N., Halas N. J., Halbout J. M., Kash J. A., and Li G. P., "Generation of sub-picosecond electrical pulses on coplanar transmission lines," Appl. Phys. Lett., **48**, 751-753 (1986).

31. Dudley J. M. et al., "Complete characterization of terahertz pulse trains generated from nonlinear processes in optical fibers," IEEE J. Quant. Electron., **37**, 587-594 (2001).

32. Zhang X. -C, Jin Y., and Ma X. F., "Coherent measurement of THz optical rectification from electro-optic crystals," Appl. Phys. Lett., **61**, 2764-2766 (1992).

33. Rice A., Jin Y., Ma X. F, Zhang X. -C., Bliss D., Larkin J., and Alexander M., "Terahertz optical rectification from <110> zinc-blende crystals," Appl. Phys. Lett., **64**, 1324-1326 (1994).

34. Schneider A., Biaggio I. and Gunter P., "Optical generation of THz pulses via optical rectification in the organic salt DAST," Opt. Commun., **224**, 337-341 (2002).

35. Bonvalet A., Joffre M., Martin J. L., and Migus A., "Generation of ultra broadband femtosecond pulses in the mid-infrared optical rectification of 15fs light pulses at 100 MHz repetition rate, Appl. Phys. Lett., **67**, 2907-2909 (1995).

36. Mourou G. A., Stancampiano C. V., Antonetti A., and Orszag A., "Picosecond microwave pulses generated with a subpicosecond laser driven semiconductor switch," Appl. Phys. Lett., **39**, 295-296 (1981).

37. Siegel P. H., "Terahertz technology in biology and medicine," IEEE Trans. Micro. Theory and Tech., **52**, 2438-2446 (2004).

38. Mickan S., Abbott D., Munch J., Zhang X. -C., and Vandoorn T., "Analysis of system trade-offs for THz Imaging," Microelec. J., **31**, 503-514 (2000).

39. Hadni A., "A short history of 50 years of research in the far-infrared: 1952-2002," Int. J. infrared and millimeter waves, **24**, 91-102 (2003).

40. Maiwal F., Martin S., Bruston J., Maestrini A., Crawford T., and Siegel P. H., "2.7 THz tripler using monolithic membrane diodes," IEEE MTT-S International Microwave Symposium Digest, 3, 1637-1640, Phoenix, AZ (2001).

41. Ryzhii V., Khmyrova I., and Shur M., "Terahertz photomixing in quantum well structures using resonant excitation of plasma oscillations," J. Appl. Phys., **91**, 1875-1881 (2002).

42. Siegel P. H., Smith R. P., Gaidis M. C. and Martin S. C., "2.5 THz GaAs monolithic membrane-diode mixer," IEEE Trans. Microwave Theory Tech., **47**, 596-604 (1999).

43. Gaidis M. C., Pickett H. M., Smith C. D., Martin S. C, Smith P. R. and Siegel P. H., "A 2.5 THz receiver front end for spaceborne applications,"IEEE Trans. Microwave Theory Tech., **48**, 733-739 (2000).

44. Carr G. L., Martin M. C., Mckinnery W. R., Jordan K., Neil G. R., and Williams G. P., "High power terahertz radiation from relativistic electrons," Nature, **420**, 153-156 (2002).

45. Morris J. R., and Shen Y. R., "Theory of far-infrared generation using optical mixing," Phys. Rev. A., **15**, 1143-1156 (1977).

46. Brown E. R., McIntosh K. A., Nichols K. B, and Dennis C. L., "Photomixing upto 3.8 THz in low temperature grown GaAs," Appl. Phys. Lett., **66**, 285-287 (1995).

47. Kohler R., Tredicucci A., Beltram F., Beere H. E., Linfield E. H., Davies A. G., Ritchie D.A., Iotti R.C., and Rossi F., "Terahertz semiconductor heterostructure laser, Nature, **417**, 156-159 (2002).

48. Kumar S., Williams B. S., Kohen S., Qing H., and Reno J. L., "Continuous-wave operation of terahertz quantum-cascade lasers above liquid-nitrogen temperatures," Appl. Phys. Lett., **84**, 2494-2496 (2004).

49. Williams B. S., Kumar S., Callebaut H., Hu Q., and Reno J. L., "Terahertz quantum-cascade laser operating up to 137 K," Appl. Phys. Lett., **83**, 5142-5144 (2003).

50. Wu Q., and Zhang X. -C., "Free space electro-optic sampling of terahertz beams," Appl. Phys. Lett., **67**, 3523-3525 (1995).

51. Liu K., Xu J., and Zhang X. -C., "GaSe crystals for broadband terahertz wave detection," Appl. Phys. Lett., **85**, 863-865 (2004).

52. Brodschelm A., Tauser F., Huber R., Sohn J. Y., and Leitenstorfer A., "Amplitude and phase resolved detection of tunable femtosecond pulses with frequency components beyond 100 THz," in T. Elsaesser, S. Mukamel, M.M. Murnane and N.F. Scherer(eds), Ultrafast Phenomena XII, Springer-Verlag, Berlin, 215-217 (2000)

53. Shen Y. C., Upadhya P. C., Linfield E. H., Beere H. E., Davies A. G., Gregory I. S., Baker C., Tribe W. R., and Evans M. J., "Generation and detection of ultrabroadband terahertz radiation using photoconductive emitters and receivers," Appl. Phys. Lett., **85**, 164-166 (2004).

54. Kono S., Tani M., and Sakai K., "Coherent detection of mid-infrared radiation upto 60 THz with an LT-GaAs photoconductive antenna," IEE Proceedings in Optoelectronics, **149**, 105-109 (2002).

55. Gaidis M. C., Pickett H. M., Smith C. D., Martin S. C., Smith R. P., and Siegel P. H., "A 2.5 THz receiver front end for spaceborne applications," IEEE Trans. Micro. Th. Tech., **48**, 733-739 (2000).

56. Komiyama S., Astaflev O., Antonov V., Kutsuwa T., and Hirai H., "A single-photon detector in the far-infrared range," Nature, **403**, 405-407 (2000).

57. Piao Z., Tani M., and Sakai K., "Carrier Dynamics and Terahertz Radiation in Photoconductive Antennas," Jpn. J. Appl. Phys., **39**, 96-100 (1999).

58. Nemec H., Pashkin A., Kuzel P., Khazan M., Schnull S., and Wilke I., "Carrier dynamics in low temperature grown GaAs studied by terahertz emission spectroscopy," J. Appl. Phys., **90**, 1303-1306 (2001).

59. Park S. G., Melloch M. R., and Weiner A. M., "Comparison of terahertz waveforms measured by electro-optic and photoconductive sampling," Appl. Phys. Lett, **73**, 3184-3186 (1998).

60. Picosecond Instrumentation. Site details some aspects of the T-Ray 2000 analytical system. Retrieved March 29, 2006 from http://www.picometrix.com/t-ray/index.html.

61. Van Exter M. and Grischkowsky D., "Optical and electronic properties of doped silicon from 0.1-2 THz," Appl. Phys. Lett, **56**, 1694-1696 (1990).

62. Morikawa O., Tonouchi M. and Hangyo M., "Sub-THz spectroscopic system using a multimode laser diode and a photoconductive antenna," Appl. Phys. Lett., **75**, 3772-3774 (1999).

63. Morikawa O., Tonouchi M. and Hangyo M., "A cross correlation spectroscopy in subterahertz region using an incoherent light source," Appl. Phys. Lett., **76**, 1519-1521 (2000).

64. Griffiths P. R. "Chemical Infra-red Fourier Transform Spectroscopy," Wiley, New York (1975).

65. Schroeder D. K., Thomas R. N. and Swartz J. C., "Free carrier absorption in silicon," IEEE Trans. Elecron. Devices, **ED-25**, 254-266 (1978).

66. Hara H. and Nishi Y., "Free carrier absorption in p-type silicon, J. Phys. Soc. Jpn, **21**, 1222-1222 (1966).

67. Dorney T. D., Baraniuk R. G. and Mittleman D. M., "Material parameter estimation using terahertz time domain spectroscopy," J. Opt. Soc. Am. A, **18**, 1562-1570 (2001).

68. Van Exter M. and Grischkowsky D., "Carrier dynamics of electrons and holes in moderately doped Silicon," Phys. Rev. B, **41**, 12140-15150 (1989).

69. Herrmann M., Tani M., Sakai K. and Fukasawa R., "Terahertz imaging of silicon wafers," J. Appl. Phys., **91**, 1247-1250 (2002).

70. Duvillaret L., Garet F. and Coutaz J. L., "A reliable method for extraction of material parameters in terahertz time domain spectroscopy," IEEE J. Select Topics Quantum Electron., **2**, 739-746 (1996).

71. Duvillaret L., Garet F. and Coutaz J. L., "Highly precise determination of optical constants and sample thickness in terahertz time domain spectroscopy," Appl. Opt., **38**, 409-415 (1999).

72. Walker G. C., Berry E., Smye S. W., Zinovev N. N., Fitzgerald A. J., Miles R. E., Chamberlain M. and Smith M. A., "Two method for modeling the propagation of terahertz radiation in a layered structure," J. Biol. Phys., **29**, 141-148 (2003).

73. Kuzel P. and Petzelt J., "Time resolved terahertz transmission spectroscopy of dielectrics," Ferroelectrics, **239**, 949-956 (2000).

74. Born M. and Wolf E., "Principles of Optics," Cambridge University Press, London, UK (1999).

75. Fox M., "Optical properties of Solids," Oxford University Press, New York, NY (2001).

76. Smith R. A. "Semiconductors," Cambridge University Press, New York, NY (1961).

77. Palik E. D. (ed.), "Handbook of Optical Constants of Solids," Academic Press, New York, NY (1997).

78. Kittel C., "Solid State Physics," John Wiley and Sons Inc., New York, NY (1995).

79. Moore G. E., "Progress in digital integrated electronics," IEEE IEDM Tech. Dig. **1**, 11-13 (1975).

80. Wilk G. D., Wallace R. M. and Anthony J. M., "High κ gate dielectrics: current status and materials properties considerations," J. Appl. Phys., **89**, 5243-5275 (2001).

81. Kingon A. I., Maria J. P. and Streiffer S. K., "Alternative dielectrics to silicon dioxide for memory and logic devices," Nature, **406**, 1032-1039 (2000).

82. Lo S. H., Buchanan D. A., Taur Y. and Wang W., "Quantum mechanical modeling of electron tunneling current from the inversion layer of ultra thin oxide n MOSFETs," IEEE Electron Device Lett., **18**, 209-211 (1997).

83. Stoneham A. M., "Why model high-k dielectrics?," J. Non Crystalline Solids, **303**, 114-122 (2002).

84. Lo W., Kamath A., Kher S., Metzner C., Wen J. and Chen Z., "Deposition and characterization of HfO_2 high *k* dielectric films," J. Mater. Res., **19**, 1775-1782 (2004).

85. Lin Y. S., Puthenkovilakam R., and Chang J. P., "Dielectric property and thermal stability of HfO_2 on silicon," Appl. Phys. Lett., **81**, 2041-2043 (2002).

86. Robertson J., "Band structures and band offsets of high K dielectrics on Si," Appl. Surf. Sc., **190**, 2-10 (2002).

87. Dakovski G. L., Kubera B., Lan S. and Shan J., "Finite pump beam size effects in optical pump-terahertz probe spectroscopy," J. Opt. Soc. Am. B., **23**, 139-141 (2006).

88. Zielbauer J. and Wegener M., "Ultrafast optical pump THz-probe spectroscopy on silicon," Appl. Phys. Lett., **68**, 1223-1225 (1996).

89. UhD Jepsen P., Schairer W., Libon I. H., Lemmer U., Hecker N. E., Birkholz M., Lips K. and Schall M., "Ultrafast carrier trapping in microcrystalline silicon in optical pump-terahertz probe measurements," Appl. Phys. Lett., **79**, 1291-1293 (2001).

90. Gusev E. P. and D'Emic C. P., "Charge detrapping in HfO_2 high k gate dielectric stacks," Appl. Phys. Lett., **83**, 5223-5225 (2003).

91. Ashcroft N. W. and Mermin N. D., "Solid State Physics," Brooks Cole, New York, NY (1976).

92. Bohren C. F. and Huffman D. R., "Absorption and Scattering of light by Small Particles," John Wiley and Sons, New York, NY (1983).

93. Philip H. R. and Ehrenrich H., "Optical properties of semiconductors," Phys. Rev., **129**, 1550-1560 (1963).

94. Altan H., Sengupta A., Federici J. F., Grebel H. and Pham D., "Estimation of defect characteristics of HfO_2 and SiO_2 on p-type silicon substrates using THz spectroscopy," J. Appl. Phys., under review (2005).

95. Altan H., "Characteristics of nanocomposites and semiconductor heterostructure wafers using THz spectroscopy," PhD Dissertation, New Jersey Institute of Technology, United States of America (2005).

96. Ramo S., Whinnery J. R. and Van Duzer R., "Fields and Waves in Communication Electronics," Wiley, New York, NY (1993).

97. Davies C. C., "Lasers and Electro-Optics," Cambridge University Press, Cambridge, UK (1996).

98. "Optical properties of Silicon." Site details optical properties of Silicon at different wavelengths. Retrieved February 17, 2006 from http://www.virginiasemi.com/pdf/Optical20Properties20of20Silicon71502.pdf

99. Abrahamson J., "Modeling Alternative High Dielectric Constant Thin Films," REU 2004 Summer Program, Advanced Materials Research Laboratory, University of Illinois at Chicago (2004).

100. Lee B. J. and Zhang B. M., "Development of experimentally validated optical property models for silicon and related materials," Proc. Of 11th IEEE International Conference on Advanced Thermal Processing of Semiconductors," **RTP 2003**, 143-150 (2003).

101. Semiconductor International, Reed Electronics Group. Site details properties of deep UV photoresist under different conditions. Retrieved October 31, 2004 from http://www.reed-electronics.com/semiconductor/article/CA41503.pdf

102. Perera A. G. U, Shen W. Z., Mallard W. C., Tanner M. O. and Wang K. L., "Far infrared free hole absorption in epitaxial silicon films for homojunction detectors," Appl. Phys. Lett., 71, 515-517 (1997).

103. Zukic M., Torr D. G., Span J. F. and Torr M. R., "Vacuum ultraviolet thin films. 1: Optical Constants of HaFBaF_2, CaF_2, LaF_3, MgF_2, Al_2O_3, HfO_2 and SiO_2 thin films," Appl. Opt., **29**, 4284-4296 (1990).

104. Boltaks B. I., "Diffusion in Semiconductors," Academic Press, New York, NY (1963).

105. Van Kranendonk J. and Sipe J. E., "Foundations of the macroscopic electromagnetic theory," Prog. Opt., **15**, 246-350 (1977).

106. Aspnes D. E., "Optical properties of thin films," Thin Solid Films, **89**, 249-262 (1982).

107. Grandqvist C. G. and Hunderi O., "Optical properties of ultrafine gold particles," Phys. Rev. B, **16**, 3513-3534 (1977).

108. Spanier J. E. and Herman I. P., "Use of hybrid phenomenological and statistical effective medium theories of dielectric functions to model the infrared reflectance of porous SiC films," Phys. Rev. B., 61, 10437-10450 (2000).

109. Schuler A., Ellenberger C., Oelhafen P., Haug C. and Brenn R., "Optical properties of titanium containing amorphous hydrogenated carbon films," J. Appl. Phys., **87**, 4285-4292 (2000).

110. Kalnin J. R. and Kotomin E., "Modified Maxwell-Garnett and Lorentz-Lorentz equations for the effective transport coefficients in inhomogeneous media," J. Phys. A: Math. Gen., **31**, 7227-7234 (1998).

111. Levy O. and Stroud D., "Maxwell-Garnett theory for mixtures of anisotropic inclusions: Application to conducting polymers," Phys. Rev. B., **56**, 8035-8056 (1997).

112. Pham D., personal communication dated August 11, 2004.

113. Chau R. S., "Intel's breakthrough in High K gate dielectric drives Moore's law well into the future," Intel Technological Magazine, **1**, 3-10 (2004).

114. Muller D. A., Sorsch T., Moccio S., Baumann F. H., Evans-Lutterodt K. and Timp G., "The electronic structure at the atomic scale of ultrathin gate oxides," Nature, **399**, 758-762 (1999).

115. Grunthaner F. J. and Grunthaner P. J., "Chemical and electronic structure of the Si/SiO_2 interface," Mater. Sci. Rep. **1**, 65-160 (1986).

116. Wang S., Ferguson B., Abbott D. and Zhang X. -C., "T-Ray Imaging and Tomography," J. Biol. Phys., **29**, 247-256 (2003).

117. Federici J. F., Schulkin B., Huang F., Gary D. E., Barat R. B., Oliviera F. and Zimdars D., "THz imaging and sensing for security applications," Semicond. Sc. Tech., **20**, S-266-S280 (2005).

118. Cook D.J. Decker B. K. and Allen M. G., "Through container THz Sensing: Applications for explosive screening," Proc. SPIE, **5354**, 55-62 (2004).

119. Kemp M.C., Cook D.J. Decker B. K. and Allen M. G., "Security applications of THz technology," Proc. SPIE, **5070**, 44-52 (2003).

120. Hermann M., Tani M., Watanabe M., and Sakai K., "Terahertz imaging of powders," IEE Proceedings-Optoelectronics, **149**, 116-120 (2002).

121. Chan T. L. J., Bjarnason J. E., Lee A. W. M., Celis M. A. and Brown E. R., "Attenuation contrast between biomolecular and inorganic materials at terahertz frequencies," Appl. Phys. Lett., **85**, 2523-2525 (2004).

122. Taday P. F., "Applications of terahertz spectroscopy to pharmaceutical sciences," Phil. Trans. R. Soc. of Lond. A, **362**, 351-364 (2004).

123. Cook D. J., Decker B. K. and Allen M. G., "Quantitative THz spectroscopy of explosive materials," Optical THz Science and Technology Topical Meeting, Orlando, FL (2005).

124. Jarzembski M. A., Norman M. L., Fuller K. A., Srivastava V. and Cutten D. R., "Complex refractive index of ammonium nitrate in the 2-20 μm spectral range," Appl. Opt., **42**, 922-930 (2003).

125. Bandyopadhyay A., Sengupta A., Barat R. B., Gary D. E. and Federici J. F., "Grain size dependent scattering studies of common materials using THz time domain spectroscopy," Proc. SPIE, 6120, 61200H (2006).

126. Van De Hulst H. E., "Light scattering by small particles," John Wiley and Sons Inc., New York, NY (1957).

127. Bandyopadhyay A., "Study of propagation and detection methods of THz radiation for spectroscopy and imaging," PhD Dissertation, New Jersey Institute of Technology, United States of America (2006).

128. Scarfi M. R., Romano M., Di Pietro R., Zeni O., Doria A., Gallerano G. P., Giovenale E., Messina G., Lai A., Campurra G., Coniglio D. and D'Arienzo M., "THz exposure of whole blood for the study of biological effects on human lymphocytes," J. Biol. Phys., **29**, 171-177 (2003).

129. Clothier R. H. and Bourne N., "Effects of THz exposure on human primary keratinocyte differentiation and viability," J. Biol. Phys., **29**, 179-185 (2003).

130. Kemp M. C., Taday P. F., Cole B. E., Cluff J. A., Fitzgerald A. J. and Tribe W. R., "Security applications of terahertz technology," Proc. SPIE, **5070**, 44-52 (2003).

131. Chen Y., Liu H., Den Y., Veksler D., Shur M., Zhang X. -C., Schauki D., Fitch M. J. and Osiander R., "Spectroscopic characterization of explosives in the far-infrared region," Proc. SPIE, **5411**, 1-8 (2004).

132. Yamamoto K., Yamaguchi M., Miyamaru F., Tani M., Hangyo M., Ikeda T., Matsushita A., Koide K., Tatsuno M. and Minami Y., "Non invasive inspection of C-4 explosive in mails by terahertz time domain spectroscopy," Jpn. J. Appl. Phys., **43**, 414-417 (2004).

133. Shen Y. C., Lo T., Taday P. F., Cole B. E., Tribe W. R. and Kemp M. C., "Detection and identification of explosives using terahertz pulsed spectroscopic imaging," Appl. Phys. Lett., **86**, 241116-241118 (2005).

134. Liu H., Chen Y., Bastiaans G. J. and Zhang X. -C., "Detection and identification of explosive RDX by terahertz diffuse reflection spectroscopy," Opt. Exp., **14**, 415-423 (2006).

135. Mills N. J., "Optical Properties," in Encyclopedia of Polymer Science and Engineering, **10**, Wiley, New York, NY (1987).

136. Lamonte R. R. and McNally D., "Uses and processing of cyclic olefin copolymers," Plastic Eng., **56**, 51-60 (2000).

137. The Handbook of Plastic Optics, US Precision Lens, Cincinnati, OH (1983).

138. Kaino T., "Polymer Optical Fibers," in Polymers for Lightwave and Integrated Optics, Hornak L.A. (ed.), Marcel Dekker, New York, NY (1992).

139. Diffractive Optics: Design, Fabrication and Applications, **11**, Optical Society of America, Washington D.C., D.C. (1994).

140. Abe Y., Matsura Y., Shi Y., Wang Y., Uyama H. and Miyagi M., "Polymer coated hollow fiber for CO_2 laser delivery," Opt. Lett., **23**, 89-90 (1998).

141. Shi Y., Abe Y., Matsura Y. and Miyagi M., "Low loss smart hollow waveguides with new polymer coating material," Opt. Laser Tech., **31**, 135-140 (1999).

142. Eldada L. and Shacklette L., "Advances in polymer integrated optics," IEEE J. Sel. Top. Quantum Electron., **6**, 54-68 (2000).

143. Shi Y., Pan Z., Matsuura Y. and Miyagi M., "New and simple method for fabricating polymer coated silver hollow fibers with large mechanical strength," Opt. Laser Tech., **32**, 273-275 (2000).

144. Polyplastics. Property of TOPAS grades. Site details properties and raw materials of cyclic olefin polymers. Retrieved February 25, 2006 from http://www.polyplastics.com/en/product/lines/topas/TOPAS.pdf

145. Shin J. Y., Park J. Y., Liu C., He J. and Kim S. C., "Chemical Structure and Physical Properties of Cyclic Olefin Copolymers," Pure Appl. Chem., **77**, 801-814 (2005).

146. Khanarian G. and Celanese H., "Optical properties of cyclic olefin copolymers," Opt. Eng., **40**, 1024-1029 (2001).